Research Square

Preprints are preliminary reports that have not undergone peer review.
They should not be considered conclusive, used to inform clinical practice,
or referenced by the media as validated information.

# Design of a Triple-Band Microstrip Patch Antenna Using Machine Learning-Assisted Prediction for Sub-6 GHz Applications

**Pauly T. B. Halweendo**
University of Namibia
**Srinu Sesham**
ssesham@unam.na
University of Namibia
**Clement Temaneh Nyah**
University of Namibia

**Research Article**

**Keywords:** Microstrip multiband antenna, Machine learning model, Optimization, CST Studio Suite, Scattering parameters, 5G FR1 Band

**Posted Date:** November 13th, 2026

**DOI:** https://doi.org/10.21203/rs.3.rs-11352777/v1

**License:** This work is licensed under a Creative Commons Attribution 4.0 International License.
Read Full License

**Additional Declarations:** No competing interests reported.

# Design of a Triple-Band Microstrip Patch Antenna Using Machine Learning-Assisted Prediction for Sub-6 GHz Applications

Pauly T. B. Halweendo, Srinu Sesham, Clement Temaneh Nyah

*Department of Electrical and Computer Engineering, University of Namibia, Ongwediva, Namibia.

*Corresponding author(s). E-mail(s): ssesham@unam.na;
Contributing authors: bhalweendo@hotmail.com; cntemaneh@unam.na;

**Abstract**

The increasing demand for compact multiband antennas in 5G/6G communications, cognitive radio, and other modern wireless communication systems requires efficient and intelligent antenna design approaches. Conventional antenna optimization methods based on full-wave electromagnetic simulations are time-consuming and computationally expensive due to repeated design iterations. Machine learning (ML)-assisted methods provide a faster prediction of optimal design/geometry parameters for efficient multiband anttena for targeted Sub-6 GHz applications. Multiband microstrip patch antennas are attractive for compact sub-6 GHz radios, but placing several resonances with full-wave simulation alone is slow. Published ML based studies mostly address one or two bands. They rarely test whether the simulated antenna meets a matching requirement at the required centre frequencies, or whether the training data are themselves consistent. This paper presents an ML-assisted workflow for a compact dual-slot, inset-fed microstrip antenna with a defected ground structure on FR-4. It targets the 2.4 GHz ISM, 3.5 GHz 5G n78 and 5.8 GHz ISM bands. A Latin Hypercube plan of 805 geometries over five parameters was simulated in CST Studio Suite, giving 630 usable samples with 15 outputs each. A first campaign was discarded after a consistency check showed unrelated outputs for identical geometries. Random forest (RF), XGBoost, and a neural network (ANN) MODELS are trained and compared, with and without electrical-length features. On 95 held-out designs, XGBoost with engineered features reached the highest mean $\boldsymbol{R^2}$ across all fifteen outputs (0.72). This compares with 0.70 for the raw ANN, 0.68 for raw XGBoost and 0.67 for RF. The surrogates also separated passing from failing designs well, with an AUC from 0.93 for the raw ANN to 0.99 for

the engineered-feature ANN. Even so, the difference between XGBoost and the neural network was within statistical noise. A surrogate-guided search followed by 40 verification simulations produced a design that meets $\boldsymbol{S_{11} \leq -10}$ dB at all three target frequencies ($\boldsymbol{-11.4}$, $\boldsymbol{-21.5}$ and $\boldsymbol{-11.6}$ dB), where the baseline meets none. Six of eight tolerance variants still met all three targets. Gain, efficiency, VSWR, coverage of the standard bands and radiation patterns are reported for the final design. The design is narrow-band with modest gain and efficiency, and all results are from simulation.

**Keywords:** Microstrip multiband antenna, Machine learning model, Optimization, CST Studio Suite, Scattering parameters, 5G FR1 Band

# Nomenclature

### Geometry and substrate

$L_p$ Patch length (mm)
$W_p$ Patch width (mm)
$L_{s2}$ Length of slot 1, associated with the 3.5 GHz band (mm)
$L_{s3}$ Length of slot 2, associated with the 5.8 GHz band (mm)
$y_0$ Inset feed depth (mm)
$h$ Substrate thickness (mm)
$W_f$ Width of the 50 Ω feed line (mm)
$W_g$, $L_g$ Overall board width and length (mm)
$\varepsilon_r$ Relative permittivity of the FR-4 substrate
$\tan\delta$ Substrate loss tangent
$\varepsilon_{\text{eff}}$ Effective permittivity of the patch
$\Delta L$ Fringing length extension (mm)
$f_0$ Design frequency used in the transmission-line equations (GHz)
$c$ Speed of light in vacuum

### Antenna performance

$S_{11}$ Reflection coefficient (dB)
$\Gamma$ Complex reflection coefficient (linear)
VSWR Voltage standing wave ratio
$G$ Gain (dBi)
$D$ Directivity (dBi)
$\eta_{\text{rad}}$ Radiation efficiency
$f_{\text{res}}^{(b)}$ Resonant frequency of band $b$ (GHz)
$f_b^*$ Target centre frequency of band $b$ (GHz)
$\text{meet}_b(\mathbf{x})$ Indicator that design $\mathbf{x}$ meets band $b$ at $f_b^*$
$\text{BW}_b$ −10 dB bandwidth of band $b$ (MHz)
$m_b$ Margin from $f_b^*$ to the nearest edge of $\text{BW}_b$ (MHz)

### Design space and dataset

$\mathbf{x}$ Design vector $(L_p, W_p, L_{s2}, L_{s3}, y_0)$
$\mathcal{X}$ Feasible set of design vectors
$\mathbf{y}(\mathbf{x})$ Simulated output vector (15 quantities per design)
$n$ Number of Latin Hypercube samples
$d$ Number of sampled parameters
$\ell_b$ Electrical-length feature for band $b$
$\lambda_{g,b}$ Guided wavelength for band $b$ (mm)

**Surrogate models and evaluation**

$T$ Number of trees in the random forest
$K$ Number of boosting rounds in XGBoost
$\hat{y}(\mathbf{x})$ Surrogate model prediction
$R^2$ Coefficient of determination
MAE Mean absolute error
RMSE Root-mean-square error
$M_{\mathrm{CC}}$ Matthews correlation coefficient
AUC Area under the ROC curve
$F_1$ Harmonic mean of precision and recall
*TP, FP, TN, FN* True/false positive and negative counts

**Surrogate-guided search and tolerance study**

$F$ Differential-evolution mutation scale factor
$CR$ Differential-evolution crossover probability
$J(\mathbf{x})$ Differential-evolution cost function
$d(\mathbf{x})$ Distance from $\mathbf{x}$ to the nearest simulated design
$E_p$ Main effect of parameter $p$ on dip frequency (MHz)

# 1 Introduction

The growth of wireless services has pushed a single handset, sensor node or access point to support several radio standards at once, and demand for efficient, compact multi-band antennas is increasing [1]. Emerging applications such as multi-band spectrum sensing and reconfigurable filtering for cognitive radio add further to this demand [2]. The sub-6 GHz range is where most of them sit. The 2.4 GHz industrial, scientific and medical (ISM) band is used by wireless local area networks and many short-range devices. The 3.3–3.8 GHz n78 band carries fifth-generation (5G) New Radio traffic. The 5.725–5.875 GHz ISM band (U-NII-3) is used by higher-rate local links [3–5]. A compact antenna that covers all three bands with one radiating element saves board area, cabling and cost. This is why multiband printed antennas remain an active research topic [6–9].

The microstrip patch antenna is the usual starting point. It is planar, light, cheap to manufacture on a printed circuit board and easy to integrate with a feed line [10]. A single rectangular patch, however, resonates in one dominant mode. Multiband behaviour is normally obtained by perturbing the geometry. Slots cut into the patch add current paths and extra resonances, and fractal boundaries pack several paths into

a small area [11]. Defected ground structures (DGS) alter the ground-plane current distribution to shift and sharpen resonances [6–8, 12]. Each of these additions introduces geometric parameters that interact with each other, so the resonances cannot be placed independently by closed-form design equations alone.

The practical route is full-wave electromagnetic (EM) simulation followed by parameter sweeps or heuristic optimisation such as genetic algorithms, particle swarm and differential evolution [13–15]. That route is accurate but slow: every candidate geometry needs its own solver run, and the number of runs grows quickly with the number of parameters. Machine-learning (ML) surrogate models offer a way round this. They are trained once on a set of simulated designs and then predict the response of a new geometry almost instantly. As a result, an optimiser can examine many thousands of designs at negligible cost [16–19].

A growing literature demonstrates this idea (Table 1). Pusuluri *et al.* trained polynomial regression, random forest and XGBoost models on HFSS data for a dual-band 5G antenna and found XGBoost the most accurate [20]. Wu *et al.* proposed an ML-assisted framework for antenna geometry optimisation [21]. Babale *et al.* applied ML to a planar wideband antenna with tri-band filtering notches [22]. Palandöken *et al.* used deep-learning surrogates to cut the cost of multiband design by roughly 40% [23]. Others target inverse design with tandem or convolutional networks [24, 25], low-dimensional surrogates [26], or gain and resonance prediction [27]. Further examples include reinforcement-learning-based topology optimisation [28], ML-assisted design for high polarisation purity [29] and decision-tree forward and inverse models of microstrip antennas [30]. Other recent work includes a neural network trained on a Taguchi-designed dataset for a dual-band millimetre-wave MIMO antenna [31]. A further example is a comparison of ML algorithms for a flexible hexagonal patch [32]. A two-layer ANN has also been used to map desired antenna characteristics directly to the dimensions of a square-ring microstrip patch, an inverse-design approach validated by fabrication and measurement [33], and regression-based machine learning has been used to verify multiband and sub-THz MIMO antennas for 6G and IoT applications [34, 35]. Broadband and multiband patch designs without ML, at sub-6 GHz and millimetre-wave frequencies, continue to be reported as well [36, 37]. Tree-based models are a common choice because tabular geometry data are small and heterogeneous, a setting in which they often match or beat neural networks [38]. The dependence of model accuracy on the amount of training data is also well documented in the related work on signal classification [39, 40].

Two gaps stand out in this body of work. First, many studies report surrogate accuracy for one or two bands, or an optimised design at its own resonance. They do not ask whether the simulated antenna actually meets a matching requirement at the required centre frequencies. A dip in the reflection coefficient that lies a few hundred megahertz from a target band does not serve that band. Second, results are seldom accompanied by checks on the training data itself, although a surrogate can only be as consistent as the simulations behind it. Both matter in practice: a design workflow is only useful if a designer can trust the predictions and the final simulated antenna.

This paper addresses those gaps for a compact triple-band antenna. The main contributions are as follows. (i) A dual-slot, inset-fed patch with a defected ground

**Table 1** Summary of related work on machine-learning-assisted and multiband patch antenna design and the gap addressed in this paper.

| Study | Antenna / task | Method and key finding | Relation to this work |
|---|---|---|---|
| Pusuluri et al. (2025) [20] | Dual-band (2.2/3.6 GHz) FR-4 inset-fed patch with CSRR in the ground plane | Polynomial regression, RF and XGBoost trained on HFSS data; XGBoost best; simulated return loss −20.37/−32.27 dB, gain 4.06 dBi | Dual-band; this work handles three bands and 15 outputs |
| Shahriar et al. (2025) [41] | Quad-band patch for 5G and 6/7 WLAN | ML-assisted return-loss optimisation | Return-loss focus; this work also models resonance, gain, directivity and efficiency |
| Babale et al. (2024) [22] | Planar wideband antenna with triband filtering notches | ML predicts S11 and efficiency well | Prediction focus; this work adds a verification loop with an exact-frequency criterion |
| Wu et al. (2024) [21] | General antenna geometry design | ML-assisted optimisation reduces simulation cost versus manual tuning | General methodology; this work adds an explicit baseline-versus-optimised comparison |
| Anto Bennet and Selvakani (2025) [42] | Microstrip antenna | ML-enhanced parameter sweeping improves performance | Single band; this work targets three bands |
| Gupta et al. (2023) [24] | Multiband antennas | Tandem neural network for inverse design | Inverse-design formulation; this work uses forward surrogates, search and CST verification |
| Palandöken et al. (2024) [23] | Multiband antenna | Deep-learning surrogate; about 40% lower computational cost; prototype measured | Reports the cost saving; this work adds exact-frequency verification, screening metrics and a tolerance study |
| Chen et al. (2025) [25] | Pixelated microstrip patch (10 × 10) | CNN surrogate trained on 150 000 simulations with binary PSO; faster convergence than GA and SA | Very large dataset and pixelated patch; this work uses 630 samples and five parameters |
| Haque et al. (2023) [27] | Quasi-Yagi antenna for the n78 band | ML for gain and resonance prediction, CST simulation and measurement | Different antenna type and band; this work covers three bands |
| Kadam and Mohite (2025) [6] | Fractal multiband patch (S and C bands) | HFSS design, measured with a VNA; no ML | No ML; this work adds a surrogate-guided search |
| Boursianis et al. (2021) [13] | Multiband patch | Nature-inspired optimisation | No trained surrogate reported |
| Dhar et al. (2025) [33] | Square-ring microstrip patch | Two-layer ANN maps desired characteristics to geometry; fabricated and measured | Inverse design for one band; this work is a forward surrogate for three bands with a staged search |
| Nirob et al. (2025) [34] | Grid-structured MIMO antenna, sub-THz/THz 6G IoT | Regression-based machine learning | Different frequency regime and antenna type; this work targets sub-6 GHz triple-band coverage |
| **This work** | FR-4 dual-slot, inset-fed, DGS patch for 2.4, 3.5 and 5.8 GHz | 630-sample CST dataset; RF, XGBoost and ANN with electrical-length features; surrogate-guided search; CST verification and tolerance study | Exact-frequency verification, surrogate limits and a dataset consistency check |

structure on FR-4 is parametrised with five geometric variables. 630 usable simulations from an 805-geometry Latin Hypercube plan are collected in CST Studio Suite. (ii) Random forest (RF), XGBoost and an artificial neural network (ANN) are compared for 15 outputs, with electrical-length features and a deployable two-stage prediction cascade. (iii) The practical usefulness of the surrogates is assessed beyond $R^2$, using classification metrics and paired bootstrap tests. (iv) A staged search, guided by the surrogates and closed by full-wave simulation, yields a design that meets $S_{11} \leq -10$ dB at 2.4, 3.5 and 5.8 GHz, followed by a tolerance study. (v) A data-consistency check is reported that led to a first simulation campaign being discarded.

The rest of the paper is organised as follows. Section 2 describes the antenna, its target bands, the design space and the formulation of the problem. Section 3 presents the methodology: sampling, simulation set-up, data cleaning, feature engineering, the three surrogate models, the evaluation metrics and the search procedure. Section 4 reports and discusses the simulation results, from data quality and surrogate accuracy to the final design and its sensitivity. Section 5 concludes and lists directions for future work.

# 2 Antenna design and problem formulation

## 2.1 Baseline geometry and target bands

The antenna is a rectangular microstrip patch on a single-layer FR-4 substrate (relative permittivity $\varepsilon_r = 4.4$, loss tangent $\tan\delta = 0.025$, thickness $h = 1.6$ mm) with 35 $\mu$m copper cladding. An inset-fed 50 $\Omega$ microstrip line of width $W_f = 3.06$ mm excites the patch. Two horizontal rectangular slots are cut into the patch: the first (length $L_{s2}$) is associated with the 3.5 GHz band and the second (length $L_{s3}$) with the 5.8 GHz band. The fundamental patch mode is designed for 2.4 GHz. A rectangular slot in the ground plane below the feed line acts as the defected ground structure. The baseline is adapted from a quad-band design in the literature [41] and re-targeted to the three bands below. The top, bottom and perspective views are shown in Fig. 1.

The antenna is meant to serve three sub-6 GHz bands. These are the 2.4 GHz ISM band (2.400–2.4835 GHz), the 5G NR n78 band (3.3–3.8 GHz) and the 5.8 GHz ISM band (5.725–5.875 GHz, also known as U-NII-3) [3–5]. The design centre frequencies are $f_1^* = 2.4$, $f_2^* = 3.5$ and $f_3^* = 5.8$ GHz. The 5.8 GHz band should not be confused with the 5.925–7.125 GHz range opened for newer wireless local area networks, which lies above it.

The starting dimensions follow the standard transmission-line model of a rectangular patch [10, 43]. For a design frequency $f_0$ the patch width is

$$W = \frac{c}{2f_0}\sqrt{\frac{2}{\varepsilon_r + 1}}, \tag{1}$$

the effective permittivity that accounts for the fringing fields is given by the Hammerstad–Jensen expression [44]

$$\varepsilon_{\text{eff}} = \frac{\varepsilon_r + 1}{2} + \frac{\varepsilon_r - 1}{2}\left(1 + \frac{12h}{W}\right)^{-1/2}, \tag{2}$$

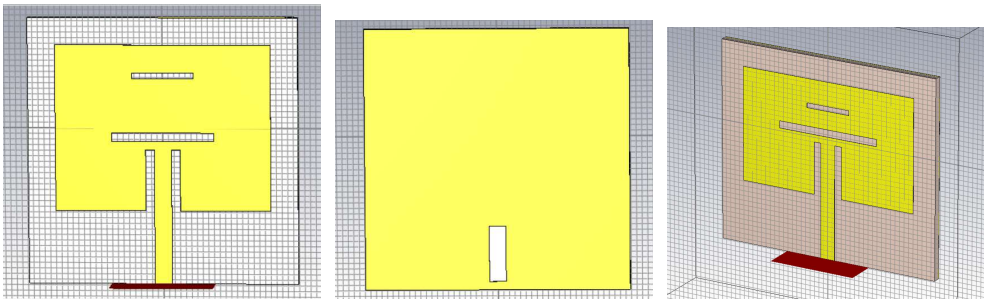
the length extension caused by the fringing at each radiating edge is

$$\Delta L = 0.412\, h\, \frac{(\varepsilon_{\text{eff}} + 0.3)\,(W/h + 0.264)}{(\varepsilon_{\text{eff}} - 0.258)\,(W/h + 0.8)}, \tag{3}$$

and the physical patch length is

$$L = \frac{c}{2 f_0 \sqrt{\varepsilon_{\text{eff}}}} - 2\,\Delta L, \tag{4}$$

where $c$ is the speed of light in vacuum. For $f_0 = 2.4$ GHz, $\varepsilon_r = 4.4$ and $h = 1.6$ mm, Eq. (1) gives $W = 38.04$ mm and Eq. (2) gives $\varepsilon_{\text{eff}} = 4.09$. Eq. (3) then gives $\Delta L = 0.74$ mm and Eq. (4) gives $L = 29.44$ mm. These are exactly the baseline values of $W_p$ and $L_p$ in Table 2, so the baseline patch is the classical 2.4 GHz design. The slots and DGS are what add the two upper bands. The slot lengths and the inset depth then control the matching and the upper resonances.



(a) (b) (c)

**Fig. 1** Baseline antenna in CST Studio Suite: (a) top view, (b) bottom view and (c) perspective view.

Figure 1 shows the geometry that all later simulations start from. In panel (a) the yellow region is the copper patch with its inset feed notch cut into the lower edge. The 50 Ω feed line enters from the bottom, and the waveguide port is the dark red plane at the end of the line. The longer of the two horizontal slots sits just above the inset and is the one associated with the 3.5 GHz band. The shorter slot near the top edge is associated with the 5.8 GHz band. Panel (b) shows the ground plane, which is continuous except for a small rectangular cut under the feed line. This defect changes the current path in the ground and is used to help pull the fundamental resonance towards 2.4 GHz. Panel (c) gives the three-dimensional arrangement, in which the

mesh lines of the simulation domain are visible behind the substrate. The overall board is slightly larger than the patch: its width is $W_g = W_p + 6h$ and its length is $L_g = L_p + 4.8 + 13$ mm. The additional 13 mm on the feed side leaves clearance for the DGS and the port. These board sizes follow the patch dimensions, so they change with the swept parameters rather than being fixed.

## 2.2 Design space

Five geometric parameters are varied: the patch length $L_p$ (which mainly sets the fundamental resonance), the patch width $W_p$, the two slot lengths $L_{s2}$ and $L_{s3}$ and the inset feed depth $y_0$ (which controls the input match). All other dimensions are held at their baseline values (Table 3). The sweep limits, chosen around the baseline, are given in Table 2. Geometric validity constraints taken from the CST model are enforced when the samples are generated: $L_p - y_0 > 10$ mm (so that the inset does not reach the first slot), $L_{s2} \le W_p - 4$ mm, $L_{s3} \le W_p - 4$ mm (slots stay inside the patch), $L_{s3} < L_{s2}$ and $y_0 > 2$ mm.

**Table 2** Design parameters, sweep limits and baseline values (all in mm).

| Parameter | Description | Min | Baseline | Max |
|---|---|---|---|---|
| $L_p$ | Patch length (fundamental resonance) | 21.0 | 29.44 | 30.0 |
| $W_p$ | Patch width | 30.0 | 38.04 | 46.0 |
| $L_{s2}$ | Slot 1 length (3.5 GHz band) | 14.0 | 18.02 | 26.0 |
| $L_{s3}$ | Slot 2 length (5.8 GHz band) | 7.0 | 10.88 | 13.0 |
| $y_0$ | Inset feed depth | 5.0 | 10.83 | 15.0 |

**Table 3** Fixed dimensions and material data of the CST model.

| Symbol | Meaning | Value | Symbol | Meaning | Value |
|---|---|---|---|---|---|
| $h$ | Substrate thickness | 1.6 mm | $W_{s2}$ | Slot 1 width | 1.5 mm |
| $t$ | Copper thickness | 0.035 mm | $W_{s3}$ | Slot 2 width | 1.0 mm |
| $W_f$ | 50 Ω feed width | 3.06 mm | $y_{s2}$ | Slot 1 centre position | 7.36 mm |
| $g$ | Inset gap (each side) | 1.53 mm | $y_{s3}$ | Slot 2 centre position | 17.67 mm |
| $L_{\mathrm{dgs}}$ | DGS slot length | 10 mm | $\varepsilon_r$ | FR-4 permittivity | 4.4 |
| $W_{\mathrm{dgs}}$ | DGS slot width | 3 mm | $\tan\delta$ | Loss tangent | 0.025 |

## 2.3 Problem formulation

Let $\mathbf{x} = (L_p, W_p, L_{s2}, L_{s3}, y_0)$ be a design vector inside the feasible set $\mathcal{X}$ of Table 2 and the constraints above. The full-wave solver defines a map $\mathbf{x} \mapsto \mathbf{y}(\mathbf{x}) \in \mathbb{R}^{15}$. For each band $b \in \{1, 2, 3\}$, its components are the minimum reflection coefficient $S_{11,\min}^{(b)}$ in a search window and the frequency $f_{\mathrm{res}}^{(b)}$ at which it occurs. The remaining components are the gain, directivity and radiation efficiency at the band. The reflection coefficient

is reported as $S_{11} = 20 \log_{10} |\Gamma|$ dB, and the voltage standing wave ratio is

$$\mathrm{VSWR} = \frac{1 + |\Gamma|}{1 - |\Gamma|}. \tag{5}$$

A matching requirement of $S_{11} \leq -10$ dB corresponds to $|\Gamma| \leq 0.316$, VSWR $\leq$ 1.92 and at most 10% of the incident power reflected. Gain, directivity and radiation efficiency are related by

$$G(\mathrm{dBi}) = D(\mathrm{dBi}) + 10 \log_{10} \eta_{\mathrm{rad}}, \tag{6}$$

so a low radiation efficiency $\eta_{\mathrm{rad}}$ lowers the gain directly.

The design goal used throughout this paper is deliberately strict. A design is said to *meet* band $b$ when the simulated $S_{11}$ read at the exact target frequency $f_b^*$ is at most $-10$ dB:

$$\mathrm{meet}_b(\mathbf{x}) = \mathbf{1}[S_{11}(f_b^*; \mathbf{x}) \leq -10\,\mathrm{dB}], \qquad b = 1, 2, 3. \tag{7}$$

The aim is to find $\mathbf{x} \in \mathcal{X}$ with $\sum_b \mathrm{meet}_b(\mathbf{x}) = 3$, using as few full-wave simulations as possible. Because the dataset stores only the deepest dip in each band window, and a deep dip can sit several hundred megahertz from $f_b^*$, Eq. (7) is stricter than the dip-depth criterion. The two are kept apart in the analysis below.

# 3 Methodology

The workflow is summarised in Fig. 2. It starts from the Design Baseline Antenna, from which a Sample Dataset of geometries is generated by Latin Hypercube sampling. The geometries are simulated in CST Studio Suite, and the results pass through Data Pre-Processing to give the Simulated Dataset, stored as a CSV file. The dataset is divided into training and test data (Train/Test) for the ML Models (RF, XGB and ANN), which yield the Optimal Geometry Parameters. These parameters are simulated again in CST Studio Suite, and the Performance of the resulting antenna (reflection coefficient and far-field pattern) is reported. Sections 3.1 to 3.6 give the details of each block.

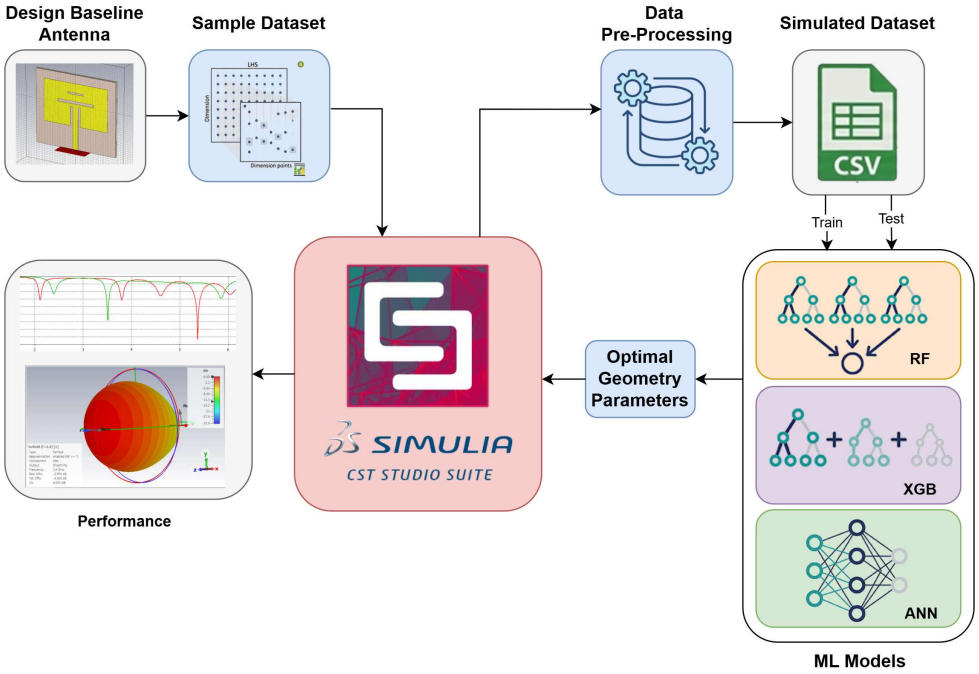



**Fig. 2** Framework of proposed ML-assisted design of triple-band microstrip patch antenna

Figure 2 shows the workflow as a single flow that passes through CST Studio Suite twice. In the top row, the Design Baseline Antenna (Section 2.1) is turned into the Sample Dataset, an 805-geometry Latin Hypercube plan over the five design parameters (Section 3.1). The plan is simulated in CST Studio Suite (Section 3.2). The extracted outputs are then cleaned in Data Pre-Processing, which removes clipped and failed runs and leaves the 630 usable samples of the Simulated Dataset, stored as a CSV file. From there the data are split into Train and Test subsets; in this study a validation subset is also held out, which gives the 70/15/15 split of Table 4. The ML Models block contains the three surrogates, RF, XGB (XGBoost) and ANN, together with the feature engineering of Section 3.3 and the evaluation metrics of Section 3.5. Their predictions are used by the differential-evolution search of Section 3.6 to propose the Optimal Geometry Parameters. The arrow back into CST Studio Suite indicates that every proposed geometry is simulated before it is trusted. In this study that second pass consists of the seven candidates and one stress test, the 24-design local batch and the eight-run tolerance study. The simulated results, not the surrogate predictions, decide which region of the design space is explored next. The last block, Performance, shows the simulated reflection coefficient and far-field pattern of the resulting antenna; the results are reported in Sections 4.6 to 4.9.

### 3.1 Latin Hypercube sampling

Latin Hypercube sampling (LHS) divides the range of each of $d$ parameters into $n$ equal-probability strata and places exactly one sample in each stratum of every parameter. As a result, all marginal ranges are covered evenly with far fewer points than a grid [45]. For sample $i$ and parameter $j$ with limits $[l_j, u_j]$,

$$x_{ij} = l_j + (u_j - l_j)\,\frac{\pi_j(i) - U_{ij}}{n}, \qquad i = 1, \ldots, n, \tag{8}$$

where $\pi_j$ is a random permutation of $\{1, \ldots, n\}$ and $U_{ij} \sim \mathcal{U}(0, 1)$. The plan combines a global block of 700 samples over the full limits of Table 2. It adds a focused block of 150 samples over a smaller sub-region around the more promising geometries. Rows that violate a validity constraint are removed and the plan is topped up until 805 feasible geometries are obtained. Fig. 3 shows how the samples are spread.

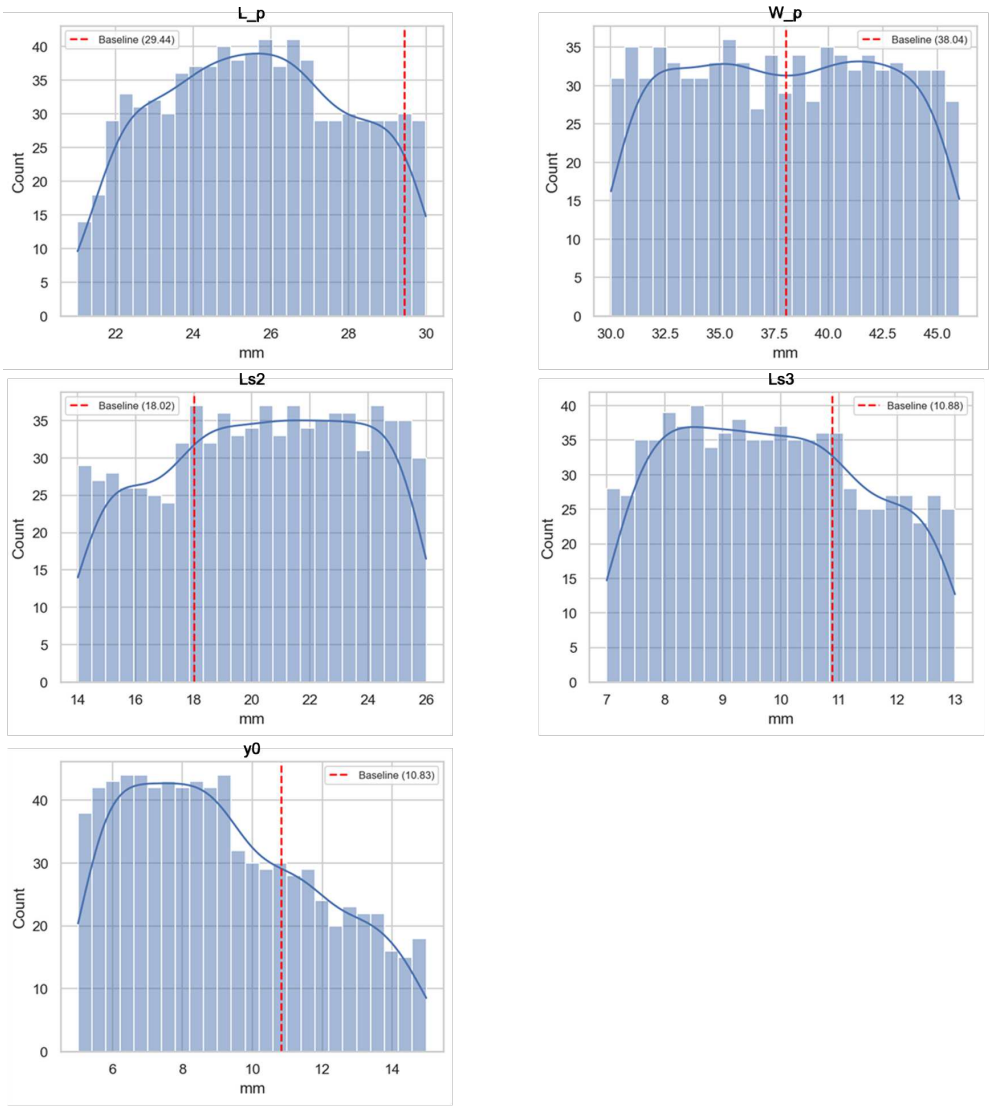



**Fig. 3** Distribution of the five design parameters in the 805-geometry Latin Hypercube plan.

Figure 3 shows one histogram per swept parameter, with a kernel density estimate drawn over the bars and the baseline value marked by a dashed red line. The patch width $W_p$ is close to uniform over 30–46 mm, which is what a Latin Hypercube produces when no constraint interferes. The other four parameters are less flat: the histograms for $L_p$, $L_{s3}$ and $y_0$ tilt towards their lower values, and $L_{s2}$ tilts towards its upper values. This tilt has two causes. The constraint $L_p - y_0 > 10$ mm removes infeasible combinations of a long inset with a short patch. The focused block also

adds samples in a smaller region at low $L_p$, low $y_0$ and high $L_{s2}$. The baseline sits inside every range but near the upper end of $L_p$ and the lower half of $L_{s2}$. As a result, the plan explores the neighbourhood of the baseline as well as shorter, more compact patches. The practical consequence is that the surrogates are best informed in the dense, lower-$L_p$ and lower-$y_0$ region. They are less well informed near the upper bound of $L_p$ where the baseline lies.

## 3.2 Electromagnetic simulation and data extraction

All geometries are simulated with the CST Studio Suite time-domain solver, which is based on the finite integration technique [46, 47]. The model has a waveguide port at the end of the feed line, open boundary conditions with padding around the antenna, a frequency sweep of 1–7 GHz and a hexahedral mesh. The licence used differs by campaign. Rounds 1 and 2 (Section 4.2) ran on the free CST Studio Suite 2026 Learning Edition, driven through its built-in GUI parameter-sweep feature, which hard-caps the mesh at 100,000 hexahedral cells for the whole simulation domain. Round 3 onward, which supplies every result in this paper, ran on the university's own commercial, node-locked CST 2023 licence, which has no mesh-cell cap and is limited only by the available hardware. Copper conductivity and the exact mesh convergence or accuracy criterion follow each licence's solver defaults and are not detailed further here. The parametrised CST model is driven in batch mode from the plan of Section 3.1, and the results table for each run is exported.

Fifteen outputs are extracted per run. For each band $b$ a search window is defined (1.8–3.0 GHz, 2.8–4.5 GHz and 4.5–7.0 GHz for bands 1, 2 and 3). Within that window, the deepest reflection minimum gives $S_{11,\min}^{(b)}$, its frequency gives $f_{\mathrm{res}}^{(b)}$ and gain, directivity and radiation efficiency are read from the far-field data at the corresponding band. A run is labelled SUCCESS when its minima lie inside their windows, and CLIPPED when a minimum sits at a window edge. In that case the true resonance lies outside the window and the value is not a real dip. It is labelled FAILED when the run did not finish. Only SUCCESS runs are used to train the surrogates. The exact-frequency criterion of Eq. (7) is applied later to the simulated $S_{11}$ curves of the search stages, which are exported in full.

## 3.3 Feature engineering

The raw inputs are the five geometry parameters. Because a resonance depends on the length of the patch measured in guided wavelengths, an electrical-length feature is added for each band,

$$\ell_b = \frac{L_p}{\lambda_{g,b}}, \qquad \lambda_{g,b} = \frac{c}{f_{\mathrm{res}}^{(b)}\sqrt{\varepsilon_{\mathrm{eff}}}}, \qquad \varepsilon_{\mathrm{eff}} \approx 3.5, \tag{9}$$

Here $\varepsilon_{\mathrm{eff}} \approx 3.5$ is the approximate effective permittivity of FR-4 at $h = 1.6$ mm. The guided wavelength is used rather than the free-space one so that the substrate enters the feature. Five dimensionless ratios are also added: slot-to-patch-width ratios $L_{s2}/W_p$ and $L_{s3}/W_p$, the inset ratio $y_0/L_p$, a slot-to-inset separation and the patch

aspect ratio. Together these give a "safe" set of 10 features that depend on geometry only.

The electrical-length features in Eq. (9) depend on the simulated resonant frequency, which is itself an output. To avoid leaking a label into the inputs, a deployable two-stage cascade is used. The resonant frequencies are predicted first from the 10 geometry-only features. The electrical-length features are then built from those *predicted* frequencies, and the remaining twelve outputs are predicted from the resulting 13 features. This is the configuration that could be used for a new geometry, and all engineered-feature results below refer to it unless stated otherwise.

## 3.4 Surrogate models

Three model families are compared. A random forest (RF) averages $T$ decision trees, each fitted to a bootstrap sample of the data with a random subset of features considered at each split, $\hat{y}(\mathbf{x}) = \frac{1}{T}\sum_{t=1}^{T} h_t(\mathbf{x})$ [48]. XGBoost builds an additive ensemble of trees, $\hat{y}(\mathbf{x}) = \sum_{k=1}^{K} f_k(\mathbf{x})$, by minimising a regularised objective

$$\mathcal{L} = \sum_i \ell\big(y_i, \hat{y}_i\big) + \sum_k \Omega(f_k), \qquad \Omega(f) = \gamma T_f + \tfrac{1}{2}\lambda\|\mathbf{w}\|^2, \tag{10}$$

where $\ell$ is the squared error, $T_f$ the number of leaves and $\mathbf{w}$ the leaf weights [49]. The artificial neural network (ANN) is a fully connected multilayer perceptron with layers $\mathbf{h}^{(l+1)} = \mathrm{ReLU}(\mathbf{W}^{(l)}\mathbf{h}^{(l)} + \mathbf{b}^{(l)})$ and a linear output layer. It is trained to minimise the mean squared error on standardised targets with the Adam optimiser [16, 17]. Table 4 lists the settings. RF and ANN models were implemented with scikit-learn and TensorFlow/Keras, XGBoost with its own library and the optimiser with SciPy [50].

**Table 4** Data split and surrogate model settings.

| Item | Setting |
|---|---|
| Data split | 630 usable samples split 70/15/15 with a fixed random seed (42): 441 training, 94 validation, 95 test designs |
| Random forest | One model per output; hyperparameters chosen by randomised search (10 draws, 5-fold cross-validation) over $n_{\text{estimators}} \in \{100, \dots, 800\}$, max_depth $\in \{\text{None}, 3, \dots, 20\}$ and the minimum leaf size |
| XGBoost | One model per output; learning rate $\in \{0.01, \dots, 0.2\}$, depth $\in \{2, \dots, 6\}$, $n_{\text{estimators}} \in \{100, \dots, 800\}$ and subsample $\in \{0.6, \dots, 1.0\}$ tuned by randomised search with 5-fold cross-validation; column subsample 0.8, $\ell_2$ weight $\lambda = 1$ |
| ANN | Multi-output: inputs $\to$ 128 $\to$ 256 $\to$ 128 $\to$ 15 (ReLU, linear output); Adam, mean-squared-error loss; inputs and outputs standardised on the training set; up to 300 epochs, early stopping on validation loss with patience 20; learning rate and batch size chosen on validation loss |
| Feature sets | Raw (5 features); safe (10 features, geometry only); full (13 features, adds the three electrical lengths from predicted resonances) |

### 3.5 Evaluation metrics

Regression accuracy is measured on the held-out test set with the mean absolute error, the root-mean-square error and the coefficient of determination,

$$\mathrm{MAE} = \frac{1}{N}\sum_{i=1}^{N}|y_i - \hat{y}_i|, \quad \mathrm{RMSE} = \sqrt{\frac{1}{N}\sum_{i=1}^{N}(y_i - \hat{y}_i)^2}, \quad R^2 = 1 - \frac{\sum_i (y_i - \hat{y}_i)^2}{\sum_i (y_i - \bar{y})^2}. \tag{11}$$

$R^2 = 0$ means the model predicts no better than the mean of the test data, and negative values mean it predicts worse than that. Because designers use $S_{11}$ mainly to decide whether a design passes $-10$ dB, a second family of metrics treats each prediction as a pass/fail decision (predicted $S_{11,\min} \le -10$ dB in every band). With true and false positives and negatives written TP, FP, TN and FN, the precision is $\mathrm{TP}/(\mathrm{TP}+\mathrm{FP})$ and the recall is $\mathrm{TP}/(\mathrm{TP}+\mathrm{FN})$. $F_1$ is their harmonic mean. The Matthews correlation coefficient is

$$M_{\mathrm{CC}} = \frac{\mathrm{TP}\cdot\mathrm{TN} - \mathrm{FP}\cdot\mathrm{FN}}{\sqrt{(\mathrm{TP}+\mathrm{FP})(\mathrm{TP}+\mathrm{FN})(\mathrm{TN}+\mathrm{FP})(\mathrm{TN}+\mathrm{FN})}} \tag{12}$$

This is used because it stays informative when the two classes are unbalanced. The area under the ROC curve (AUC) measures how well the predicted $S_{11}$ ranks passing above failing designs regardless of the threshold. A model that predicts "pass" for every design serves as the baseline classifier. Differences between models are tested with a paired bootstrap that resamples the test designs 2000 times and reports the 95% interval of the difference.

### 3.6 Surrogate-guided design search

The search has three stages, which together with their CST verification produce the Optimal Geometry Parameters and the Performance blocks of Fig. 2. In the first, the engineered-feature XGBoost model and an ANN trained on $S_{11}$ only are averaged, and differential evolution (DE) minimises a robust cost. For a population member $\mathbf{x}_i$, DE forms a mutant $\mathbf{v}_i = \mathbf{x}_{r_1} + F(\mathbf{x}_{r_2} - \mathbf{x}_{r_3})$ from three other members and builds a trial vector by binomial crossover with probability $CR$. The trial replaces $\mathbf{x}_i$ if its cost is lower. The cost is

$$\begin{aligned} J(\mathbf{x}) = {} & \max\Big(\max_b \tilde{s}_b(\mathbf{x}),\, -18\Big) + 10\sum_{b=1}^{3}\max\big(0,\, |\hat{f}_b(\mathbf{x}) - f_b^*| - 0.15\big) \\ & + 60\,\frac{\max(0,\, d(\mathbf{x}) - d_{90})}{d_{90}} + 1000\,\mathbf{1}[\mathbf{x}\notin\mathcal{X}]\,, \end{aligned} \tag{13}$$

with the robust per-band prediction $\tilde{s}_b = \bar{s}_b + 0.5\,|\hat{s}_b^{\mathrm{XGB}} - \hat{s}_b^{\mathrm{ANN}}|$, where $\bar{s}_b$ is the mean of the two model predictions. The first term rewards a deep predicted match but caps the reward at $-18$ dB. It also adds half the disagreement between the two models, so that designs on which the models disagree are penalised. The second term

penalises predicted resonances $\hat{f}_b$ more than 0.15 GHz from a target. The third term keeps the search inside the region supported by simulated data. Here $d(\mathbf{x})$ is the range-normalised distance to the nearest simulated design, and $d_{90}$ is the 90th percentile of the same distance among the simulated designs. The last term enforces the geometric constraints. Sixteen independent DE runs (population $15\times5 = 75$, 120 generations) are performed. The best members are pooled, and eight well-separated candidates (normalised separation of at least 0.22) are chosen for CST verification: seven candidates and one stress-test design, the unconstrained optimum.

Because the surrogates locate the first resonance much better than the second and third, the second stage is local. The twelve simulated designs whose three resonances lie closest to the targets are used as anchors. A Sobol sequence of 8192 points is drawn in the anchors' bounding box, expanded by 20% of each parameter range. These points are then screened with the surrogates (tight for band 1, loose for band 2, band 3 left free), and 24 designs are selected by maximin (farthest-point) spacing. In the third stage, the first design that meets all three targets is perturbed in a $2^{5-2}$ fractional-factorial experiment of eight runs. The steps are $\pm0.15$ mm in $L_p$, $W_p$, $L_{s2}$ and $y_0$, and $\pm0.09$ mm in $L_{s3}$. The main effect of parameter $p$ on the frequency $f$ of a dip is estimated as

$$E_p = \bar{f}\big|_{p=+} - \bar{f}\big|_{p=-}, \tag{14}$$

the difference between the mean dip frequency of the runs with the parameter at its high and low step. Two further quantities describe each simulated band. The first is the $-10$ dB width $\mathrm{BW}_b$, the width of the contiguous frequency interval around $f_b^*$ where $S_{11} \le -10$ dB; the second is the margin $m_b$, the distance from $f_b^*$ to the nearest edge of that interval.

# 4 Simulation results and discussion

## 4.1 Baseline performance

The baseline is simulated first. Its reflection minima fall at 2.11, 3.80 and 5.37 GHz, with depths of $-15.4$, $-15.9$ and $-41.7$ dB, that is, 0.29, 0.30 and 0.43 GHz away from the three targets. Read at the target frequencies themselves, the baseline gives only $-1.3$, $-1.6$ and $-5.4$ dB (from the digitised CST curve, accuracy about $\pm0.2$ dB). It therefore meets none of the three requirements of Eq. (7). The baseline therefore has the right number of resonances but not the right frequencies, which is the gap that the search must close. This baseline curve appears together with the optimised one in Fig. 10.

## 4.2 Dataset and data-consistency check

Table 5 summarises the simulation campaigns. A pilot campaign (Round 1) produced 261 usable samples. The 805-geometry plan of Section 3.1 was then simulated twice. The first campaign (Round 2) yielded 600 usable samples, and after the results were found to be inconsistent, the plan was re-simulated (Round 3). Round 3 completed 806 runs (the plan plus the baseline). Of these, 630 are SUCCESS, 172 are CLIPPED

(131 in band 2, 30 in band 3 and 11 in both) and 4 FAILED. Only the 630 usable runs are used below.

**Table 5** Simulation campaigns.

| Campaign | Runs | Usable | Comment |
|---|---|---|---|
| Round 1 | – | 261 | Pilot, narrow limits, no geometric constraints; superseded |
| Round 2 | 805 planned | 600 | First campaign of the 805-geometry plan; outputs found inconsistent (Fig. 4); not used for the final results |
| Round 3 | 806 | 630 | Same plan plus baseline; 172 clipped and 4 failed runs removed; used for all results |
| Verification | 40 | – | 8 global candidates, 24 local designs, 8 tolerance runs (Section 4.6) |

A consistency check exposed a problem with Round 2. For the 480 geometries present in both cleaned datasets, the outputs of the two campaigns should agree, since the geometry is the same. Figure 4 shows that they do not.

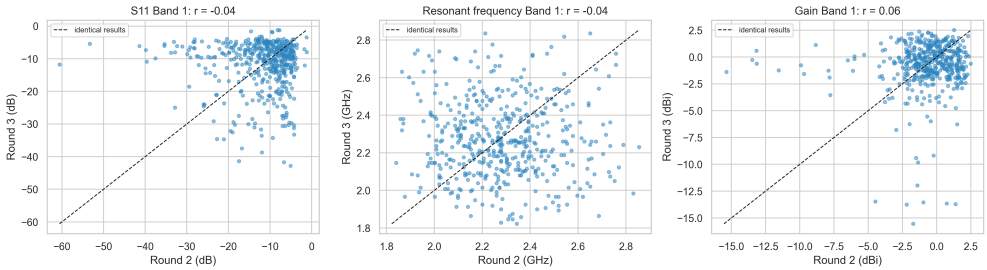



**Fig. 4** Outputs of Round 2 and Round 3 for 480 identical geometries: (a) $S_{11,\min}$ in band 1, (b) resonant frequency of band 1 and (c) gain in band 1.

In Fig. 4 each point is one geometry, with its Round 2 result on the horizontal axis and its Round 3 result on the vertical axis. If the two campaigns reproduced each other, the points would lie on the dashed diagonal. They do not. The first-band resonant frequency, for instance, is scattered over the whole 1.8–2.9 GHz range in both rounds, with a correlation of $-0.04$. The correlation of the first-band $S_{11,\min}$ is also $-0.04$, and that of the first-band gain is $+0.06$. A physical check tells which campaign to trust. A longer patch must resonate at a lower frequency, and the correlation between $f_{\text{res}}^{(1)}$ and $L_p$ is $-0.68$ in Round 3 but $+0.04$ in Round 2. The strongest correlation between any geometry parameter and any output is 0.12 in Round 2 and 0.68 in Round 3. The Round 2 outputs therefore do not follow the physics of the antenna. The cause is a licence-edition difference, not simply a different plan or a pairing error. Round 2 ran on

the free CST Studio Suite 2026 Learning Edition, hard-capped at 100,000 hexahedral mesh cells for the whole domain and driven through CST's built-in parameter-sweep feature (Section 3.2). Round 3 ran on the university's own commercial, node-locked CST 2023 licence, which has no mesh-cell cap. The triple-band geometry needs sub-millimetre mesh resolution to separate three close-lying resonances, so the capped mesh in Round 2 plausibly under-resolves $S_{11}$ and $f_{\mathrm{res}}$ and accounts for the instability seen between nominally identical geometries. This replaces an earlier interpretation that attributed the difference to mesh discretisation noise while describing both rounds as run on the same software; Rounds 1 and 2 and Round 3 onward in fact used different licence editions with different mesh-cell limits. Round 2 is retained only for this comparison.

## 4.3 Surrogate accuracy

Figure 5 compares the predictive skill of gradient-boosted trees on the three campaigns, grouped by output type.

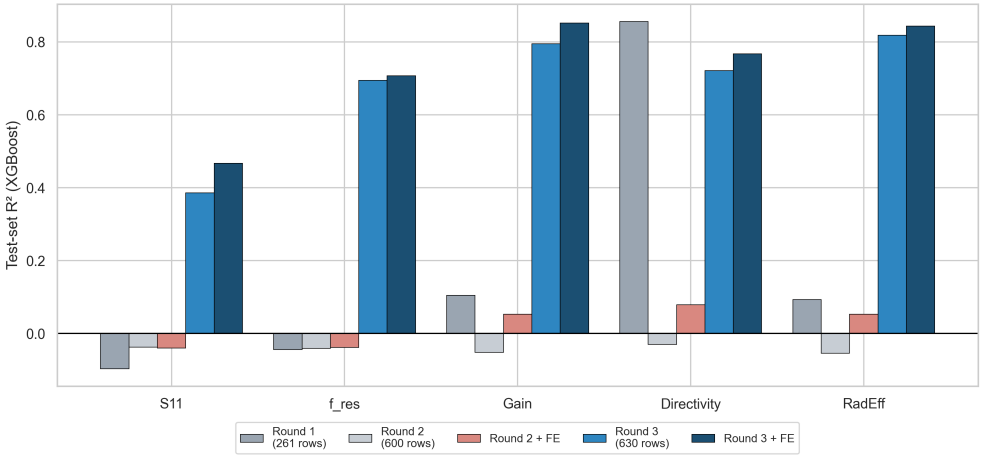



**Fig. 5** Test-set $R^2$ of XGBoost by output group for each campaign, without and with engineered features (FE).

The engineered-feature bars in Fig. 5 use electrical lengths computed from the simulated resonant frequencies, so they are an upper bound for the deployable cascade reported in Table 6. The bars are the mean $R^2$ over the three bands of each output group, and the zero line means "no better than predicting the mean". For Rounds 1 and 2 nearly every bar is at or below zero. The only large positive bar is directivity in the small pilot campaign (0.86), and Round 2, with 600 samples, is not better than Round 1 with 261. For Round 3 all groups are clearly positive. The engineered features also add a small further gain (from 0.386 to 0.467 for $S_{11}$, 0.694 to 0.707 for resonant frequency, 0.794 to 0.852 for gain, 0.721 to 0.767 for directivity and 0.818 to 0.843 for radiation efficiency). The largest values, above 0.8, occur for gain and

radiation efficiency. $S_{11}$ is the hardest output, with an $R^2$ below 0.5. The comparison also shows that data quantity is not the issue. The Round 3 campaign has about the same number of samples as Round 2 but a completely different level of predictability.

Table 6 gives the held-out results of all candidate models on Round 3 with the deployable cascade for the engineered-feature models. Table 7 lists the per-output errors of the engineered-feature XGBoost model.

**Table 6** Test-set $R^2$ (mean over the three bands) of the candidate surrogates on Round 3 (95 designs). FE = electrical-length features in the deployable cascade.

| **Output group** | **RF** | **XGBoost** | **ANN** | **XGBoost + FE** | **ANN + FE ($S_{11}$ only)** |
|---|---|---|---|---|---|
| $S_{11,\min}$ | 0.401 | 0.386 | 0.371 | 0.437 | 0.450 |
| Resonant frequency | 0.688 | 0.694 | 0.646 | 0.707 | – |
| Gain | 0.759 | 0.794 | 0.882 | 0.843 | – |
| Directivity | 0.693 | 0.721 | 0.687 | 0.759 | – |
| Radiation efficiency | 0.785 | 0.818 | 0.888 | 0.842 | – |
| **Mean over 15 outputs** | 0.665 | 0.683 | 0.695 | 0.717 | – |
| Mean $S_{11}$ MAE (dB) | 4.57 | 4.67 | 4.93 | 4.41 | 4.43 |

**Table 7** Per-output test errors of the engineered-feature XGBoost surrogate (deployable cascade, 95 test designs).

| **Output** | **Unit** | **MAE** | **RMSE** | $\boldsymbol{R^2}$ |
|---|---|---|---|---|
| $S_{11,\min}$, band 1 | dB | 1.972 | 3.679 | 0.763 |
| $S_{11,\min}$, band 2 | dB | 4.958 | 7.507 | 0.327 |
| $S_{11,\min}$, band 3 | dB | 6.291 | 9.040 | 0.219 |
| $f_{\mathrm{res}}$, band 1 | GHz | 0.015 | 0.018 | 0.992 |
| $f_{\mathrm{res}}$, band 2 | GHz | 0.157 | 0.243 | 0.623 |
| $f_{\mathrm{res}}$, band 3 | GHz | 0.327 | 0.457 | 0.506 |
| Gain, band 1 | dBi | 0.442 | 0.839 | 0.915 |
| Gain, band 2 | dBi | 0.315 | 0.484 | 0.930 |
| Gain, band 3 | dBi | 0.671 | 0.898 | 0.684 |
| Directivity, band 1 | dBi | 0.050 | 0.147 | 0.687 |
| Directivity, band 2 | dBi | 0.214 | 0.369 | 0.861 |
| Directivity, band 3 | dBi | 0.479 | 0.601 | 0.728 |
| Radiation efficiency, band 1 | % | 1.501 | 2.241 | 0.936 |
| Radiation efficiency, band 2 | % | 0.894 | 1.374 | 0.957 |
| Radiation efficiency, band 3 | % | 3.316 | 4.171 | 0.632 |

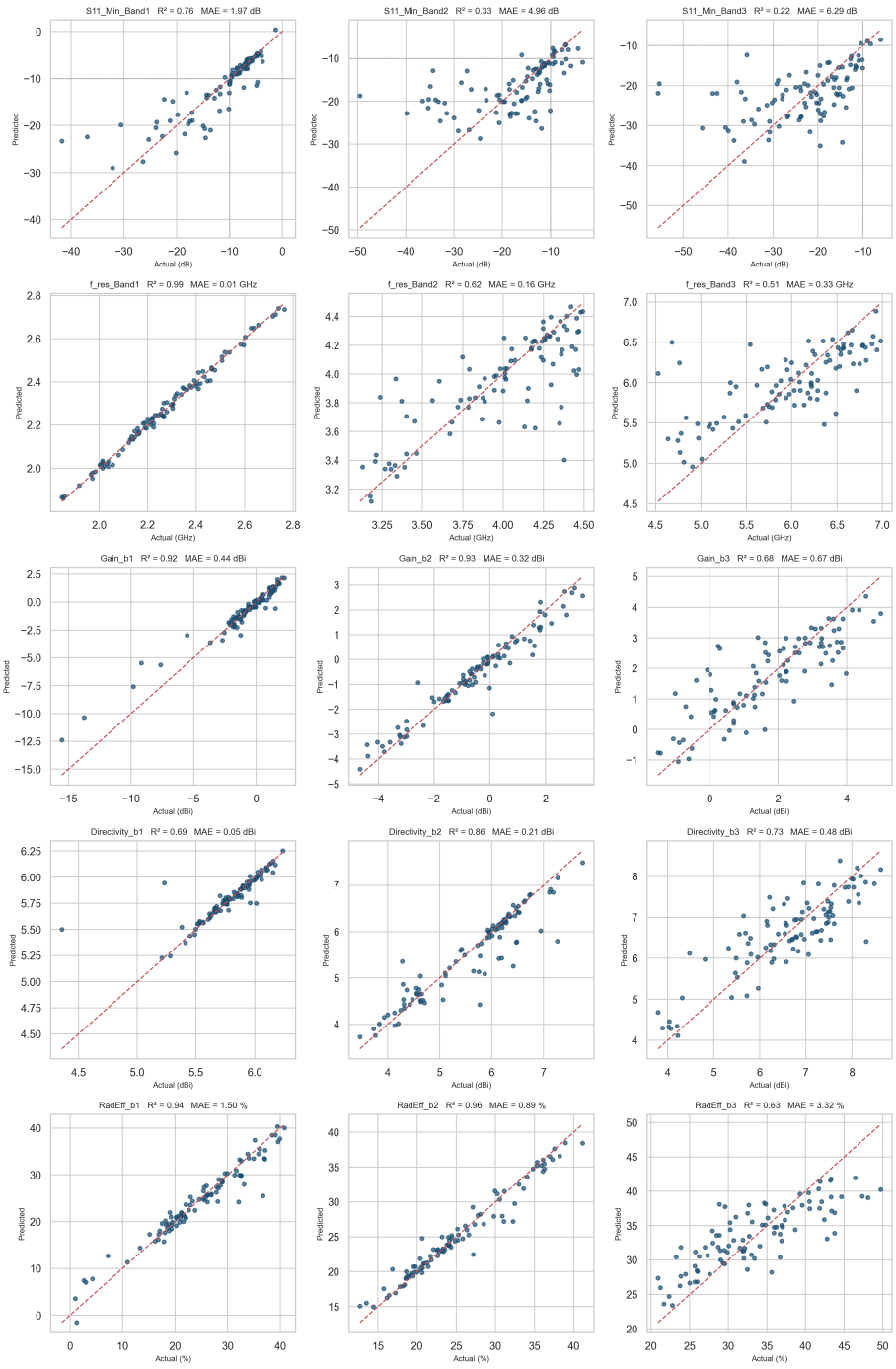



**Fig. 6** Predicted versus simulated values on the 95 test designs for all 15 outputs (rows: $S_{11,\min}$, resonant frequency, gain, directivity, radiation efficiency; columns: bands 1–3), engineered-feature XGBoost with the deployable cascade.

Figure 6 shows the test-set behaviour of the engineered-feature XGBoost model for every output. Points on the dashed diagonal are perfect predictions. The first-band resonant frequency lies almost exactly on the diagonal ($R^2 = 0.99$, MAE 0.015 GHz), which is why the first band is easy to place. The second- and third-band resonant frequencies scatter widely ($R^2 = 0.62$ and 0.51, MAE 0.16 and 0.33 GHz). This is the main reason why the surrogates cannot steer bands 2 and 3 accurately. Gain and radiation efficiency in bands 1 and 2 are close to the diagonal ($R^2$ between 0.92 and 0.96), while band 3 is noisier. The $S_{11}$ panels show that predictions are accurate for shallow matches near $-5$ to $-10$ dB in band 1, but that deep minima are under-predicted in depth. The model rarely predicts values below $-30$ dB when the simulation gives $-40$ dB or more. The dotted lines mark the $-10$ dB threshold; most points fall in the correct quadrant for band 1 but many in bands 2 and 3 are not. These band-to-band differences are quantified in Table 7.

Among the five candidate configurations the differences are small. The engineered-feature XGBoost has the highest mean $R^2$ over the 15 outputs (0.717). This compares with 0.695 for the raw ANN, 0.683 for raw XGBoost and 0.665 for the raw random forest. The $S_{11}$-only ANN with engineered features has the highest $S_{11}$ score (0.45). However, a paired bootstrap on the test set (Table 8) shows that most of these differences are not distinguishable from zero. The difference between the ANN and XGBoost with engineered features is $+0.02$ dB in $S_{11}$ MAE (95% interval $-0.47$ to $+0.43$ dB), so the two are equivalent within noise. The benefit of engineered features for XGBoost is favoured by the point estimates ($-0.27$ dB in MAE, $+0.051$ in $R^2$), but the intervals include zero. As a result, it is not statistically established at this test-set size. Only the comparison of engineered XGBoost with the raw ANN in $S_{11}$ MAE excludes zero. The ranking of models proved fragile in practice. After two valid simulations were restored to the dataset, the recommended model changed from the ANN to XGBoost. This again indicates that the choice between them is a matter of convenience, not evidence. Taking the full picture together, the engineered-feature XGBoost model is the best overall choice for this task. It has the highest mean $R^2$ across all fifteen outputs, and it is the only configuration trained for every output rather than $S_{11}$ alone. Its $S_{11}$ accuracy is also statistically indistinguishable from the neural network's at this sample size, so the added complexity of a neural network buys no established gain in return. This agrees with the general observation that tree-based models are competitive on small tabular data sets [38].

## 4.4 Parameter influence

Figure 7 shows how much each parameter contributes to the predictions, as the share of the importance of the random forest and XGBoost models, and every row sums to one. The resonant frequency is influenced mainly by the patch length (0.27), with the patch width (0.24) and the first slot length (0.25) almost as strong. This agrees with the physics that the patch length sets the fundamental resonance while the slot loads it. Gain, directivity and radiation efficiency depend most on the patch width (0.34, 0.49 and 0.32). A wider patch is a larger radiating aperture, so the directivity should depend on it most. The reflection coefficient is the only output where the inset depth is the largest contribution (0.32), which fits its role as the impedance-matching

**Table 8** Paired bootstrap comparison of $S_{11}$ accuracy on the test set (2000 resamples, mean over the three bands).

| Comparison (A − B) | $S_{11}$ metric | Difference | 95% interval | Excludes zero |
|---|---|---|---|---|
| ANN+FE − XGB+FE | MAE (dB) | +0.02 | [−0.47, +0.43] | no |
| ANN+FE − XGB+FE | $R^2$ | +0.013 | [−0.102, +0.113] | no |
| XGB+FE − XGB | MAE (dB) | −0.27 | [−0.56, +0.03] | no |
| XGB+FE − XGB | $R^2$ | +0.051 | [−0.007, +0.104] | no |
| ANN − XGB | MAE (dB) | +0.26 | [−0.17, +0.72] | no |
| ANN − XGB | $R^2$ | −0.015 | [−0.117, +0.069] | no |
| XGB+FE − ANN | MAE (dB) | −0.53 | [−0.94, −0.10] | yes |
| XGB+FE − ANN | $R^2$ | +0.065 | [−0.010, +0.157] | no |

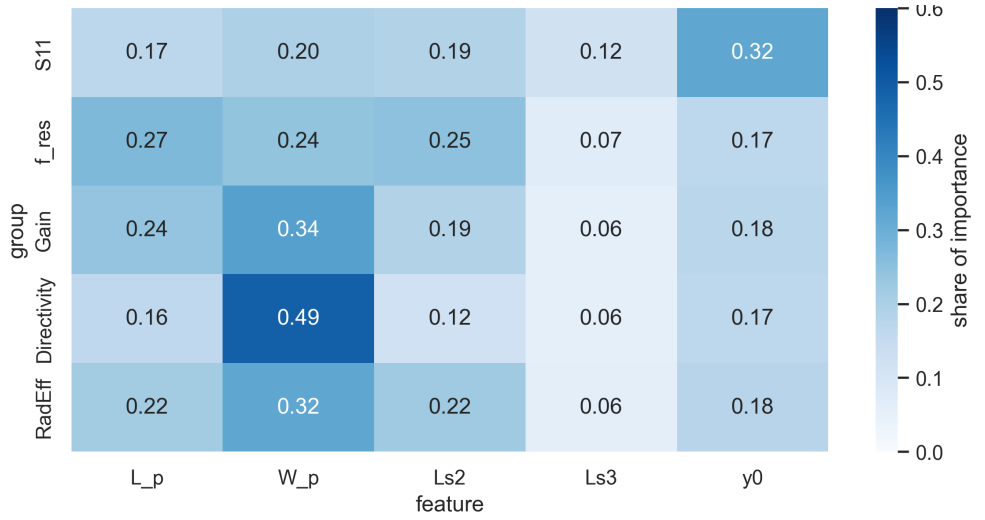



**Fig. 7** Share of importance of each geometric parameter by output group (mean of random forest and XGBoost impurity-based importances).

parameter. The second slot length $L_{s3}$ has the lowest importance in every group (0.06–0.12), so it is the least useful of the five variables for steering these outputs. The tolerance study in Section 4.9 confirms this. Importance values describe the fitted models and not causation, and impurity-based importances tend to favour continuous variables. As a result, the ranking is best read as a guide to which parameters deserve the finest control.

## 4.5 Practical usefulness of the surrogates

The $R^2$ values above do not say whether a surrogate can be used to choose designs. To test this, the surrogates were used as pass/fail screens for designs that reach −10 dB

in all three band windows; 29% of the 95 test designs do. The always-pass baseline scores an $F_1$ of 0.46. Table 9 shows that every candidate is better than this: none is a degenerate classifier, and each predicts "fail" for 48–65% of designs. The $S_{11}$-only ANN with engineered features is the best overall choice for this screening task: it leads or ties for the lead on every metric in Table 9 (accuracy 0.94, precision 0.82, recall 1.00 tied with raw XGBoost, $F_1$ 0.90, $M_{\mathrm{CC}}$ 0.87, AUC 0.99). XGBoost with engineered features is second on AUC (0.98). Keeping the top 20% of test designs ranked by predicted worst-band $S_{11}$ gives a precision of 0.89–1.00, three times the pass rate of randomly chosen designs.

**Table 9** Pass/fail screening on the test set: a design passes when the predicted $S_{11,\mathrm{min}}$ is at most −10 dB in all three bands (29% of the 95 test designs pass).

| Configuration | Acc. | Prec. | Recall | $F_1$ | $M_{CC}$ | AUC | Pred. fail (%) |
|---|---|---|---|---|---|---|---|
| RF | 0.76 | 0.55 | 0.96 | 0.70 | 0.58 | 0.98 | 48 |
| XGBoost | 0.87 | 0.70 | 1.00 | 0.82 | 0.76 | 0.97 | 58 |
| ANN | 0.82 | 0.67 | 0.79 | 0.72 | 0.60 | 0.93 | 65 |
| XGBoost + FE | 0.88 | 0.74 | 0.93 | 0.83 | 0.75 | 0.98 | 63 |
| ANN + FE ($S_{11}$ only) | 0.94 | 0.82 | 1.00 | 0.90 | 0.87 | 0.99 | 64 |
| Always-pass rule | 0.29 | 0.29 | 1.00 | 0.46 | 0.00 | 0.50 | 0 |

Figure 8 plots the true-positive rate against the false-positive rate as the decision threshold on the predicted $S_{11}$ is swept. The dashed diagonal marks a classifier with no discrimination, so a curve that hugs the upper-left corner is a good ranking of passing above failing designs. All curves are far above the diagonal. Band 1 is ranked almost perfectly (AUC 0.98–1.00, lowest for the raw ANN and highest for the engineered-feature ANN), as is band 3 (AUC 0.96–1.00, lowest for the engineered-feature ANN and highest for RF). Band 2 is somewhat harder (AUC 0.91–0.98, lowest for raw XGBoost and highest for the engineered-feature ANN). The combined curve, which corresponds to requiring a pass in every band, has AUC values from 0.93 (raw ANN) to 0.99 (engineered ANN). The steps in the curves reflect the small test set. In band 3, for example, only a few test designs fail, so the curves have few steps and the AUC is sensitive to single designs. It is important to read these results correctly. They show that the surrogates can *screen* designs on the basis of whether the deepest dip in each window reaches −10 dB, which is useful for discarding poor designs cheaply. They do not show that a design passes at the target *frequency*, which is the stricter criterion of Eq. (7); that is examined next.

## 4.6 Design search and verification

Table 10 and Fig. 9 summarise the three search stages by the number of designs that meet the exact-frequency requirement in 0, 1, 2 or 3 bands.

Figure 9 shows how the number of satisfied targets grows over the stages. Colours give the number of bands (0–3) met by each simulated design, and the numbers inside the bars give counts. The baseline (one design) meets none of the targets. Among the

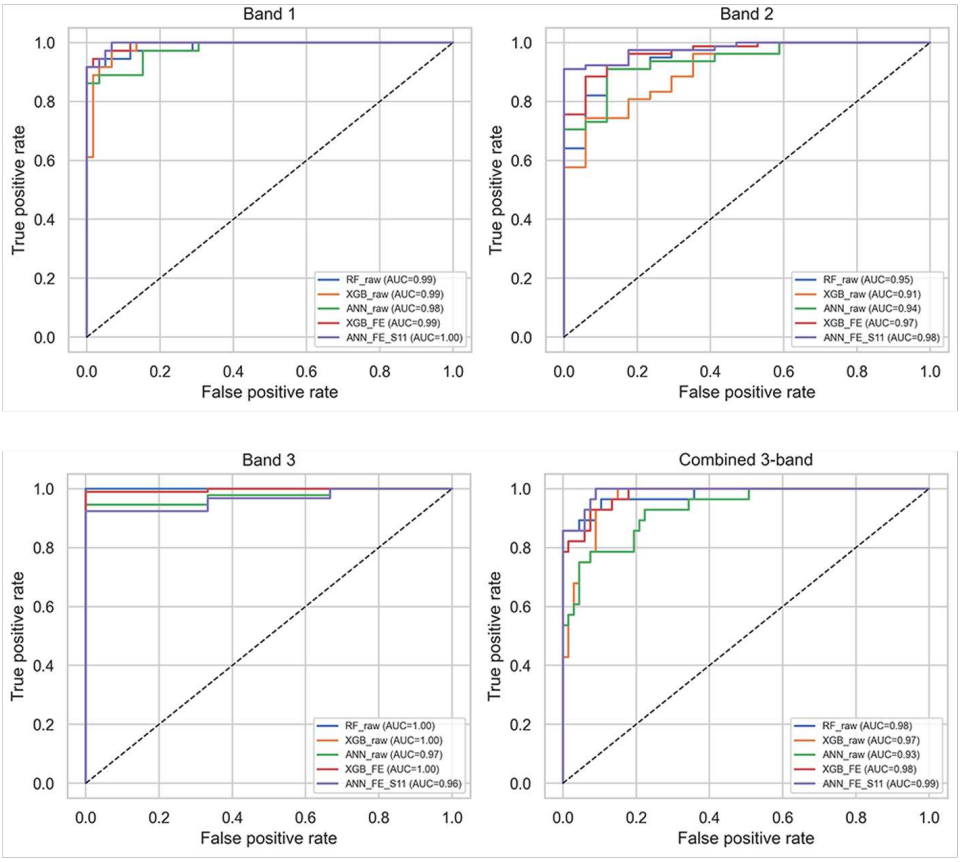



**Fig. 8** Receiver operating characteristic curves for the pass/fail decision at −10 dB, per band and combined, for the five candidate configurations.

eight designs of the first, global-surrogate stage, five meet none, two meet one and one meets two targets. All eight, however, reach −10 dB somewhere in each band window. The window minimum was therefore too lenient, and the surrogates' apparent success at screening did not carry over to the exact frequency. In the second stage, only one of the 24 local designs, called L10, meets all three targets; 13 meet none and 10 meet one. In the third stage, the eight perturbations of L10 mostly retain the property: six meet all three and two meet two. The stage-by-stage numbers reveal the search economy. About 40 simulations were needed, compared with the 805 of the initial plan. Table 11 also shows why the last stage was simulation-led. For L10 the global surrogates placed the first resonance to within 0.024 GHz, but misplaced the third by 0.6 GHz (6.47 GHz predicted, 5.85 GHz simulated) and the second-band $S_{11}$ depth by 8 dB. The final design was therefore found by local simulation that was guided by, but not predicted by, the surrogates.

**Table 10** Number of designs meeting $S_{11} \leq -10$ dB at the exact target frequencies: by number of bands met (columns 3–6) and by band (columns 7–9).

| Stage | Designs | 0 bands | 1 | 2 | 3 | 2.4 GHz | 3.5 GHz | 5.8 GHz |
|---|---|---|---|---|---|---|---|---|
| Baseline | 1 | 1 | 0 | 0 | 0 | 0 | 0 | 0 |
| Global surrogate candidates | 8 | 5 | 2 | 1 | 0 | 0 | 2 | 2 |
| Local batch | 24 | 13 | 10 | 0 | 1 | 9 | 2 | 2 |
| Tolerance batch | 8 | 0 | 0 | 2 | 6 | 8 | 8 | 6 |

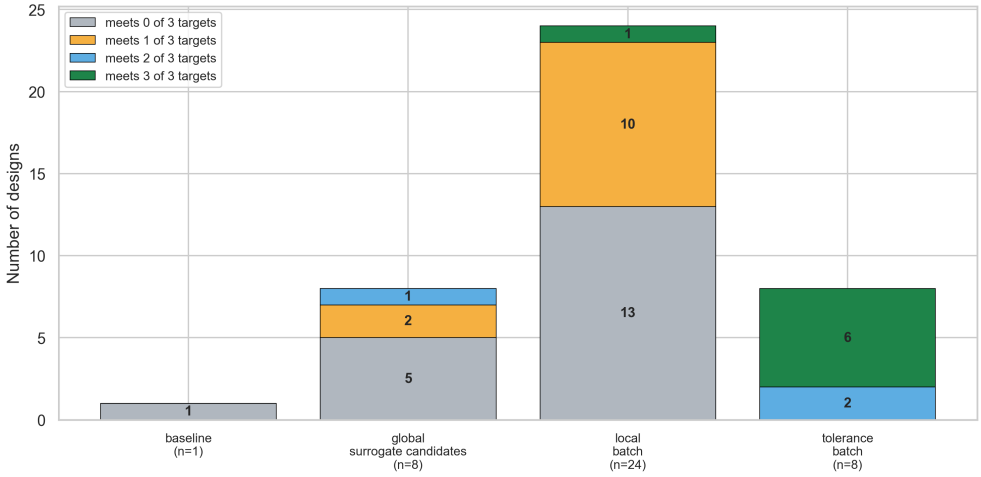



**Fig. 9** Designs meeting $S_{11} \leq -10$ dB at exactly 2.4, 3.5 and 5.8 GHz, by search stage.

**Table 11** Surrogate prediction (made at design time by the global models) versus CST for the final design L10: window-minimum $S_{11}$ in dB and resonant frequency in GHz. The models used for this prediction were trained on 628 of the 630 usable runs.

| Band | $S_{11}$ pred. | $S_{11}$ CST | Error (dB) | $f_{\text{res}}$ pred. | $f_{\text{res}}$ CST | Error (GHz) |
|---|---|---|---|---|---|---|
| Band 1 | −13.3 | −11.5 | 1.8 | 2.374 | 2.398 | 0.024 |
| Band 2 | −21.0 | −29.1 | −8.1 | 3.648 | 3.514 | −0.134 |
| Band 3 | −14.2 | −14.5 | −0.3 | 6.470 | 5.854 | −0.616 |

## 4.7 Final design

Design L10 is the only design of the local batch that meets all three targets. Among the seven designs of the whole search that do so, it also has the largest worst-band margin (22 MHz, against at most 16 MHz for the tolerance variants). Its parameters are compared with the baseline in Table 12, together with its simulated performance. Relative to the baseline, the patch is 1.9 mm shorter and 2.4 mm wider, the slots are shorter by 2.8 and 3.8 mm and the inset is 5.4 mm shallower. $y_0 = 5.48$ mm and

$L_{s3}$ = 7.09 mm lie close to the lower limits of the design space (5.0 and 7.0 mm), which suggests that the optimum may be partly limited by the chosen limits.

**Table 12** Baseline versus final design L10: geometry and simulated performance at the target frequencies. Baseline $S_{11}$ values are digitised from a CST screenshot (about ±0.2 dB); L10 values are exact CST exports. Coverage is the share of the band that lies below −10 dB.

| **Quantity** | **Unit** | **Baseline** | **L10** |
|---|---|---|---|
| $L_p$ | mm | 29.44 | 27.542 |
| $W_p$ | mm | 38.04 | 40.446 |
| $L_{s2}$ | mm | 18.02 | 15.217 |
| $L_{s3}$ | mm | 10.88 | 7.091 |
| $y_0$ | mm | 10.83 | 5.477 |
| $S_{11}$ at 2.4 GHz | dB | −1.3 | −11.4 |
| $S_{11}$ at 3.5 GHz | dB | −1.6 | −21.5 |
| $S_{11}$ at 5.8 GHz | dB | −5.4 | −11.6 |
| VSWR at 2.4 GHz | – | 13.32 | 1.73 |
| VSWR at 3.5 GHz | – | 10.95 | 1.18 |
| VSWR at 5.8 GHz | – | 3.33 | 1.72 |
| −10 dB width at 2.4 GHz | MHz | 0 | 48 |
| −10 dB width at 3.5 GHz | MHz | 0 | 90 |
| −10 dB width at 5.8 GHz | MHz | 0 | 150 |
| Margin at 2.4 GHz | MHz | 0 | 22 |
| Margin at 3.5 GHz | MHz | 0 | 34 |
| Margin at 5.8 GHz | MHz | 0 | 24 |
| Coverage of 2.4–2.4835 GHz band | % | 0 | 29 |
| Coverage of 3.3–3.8 GHz band | % | 8 | 19 |
| Coverage of 5.725–5.875 GHz band | % | 0 | 68 |
| Gain at 2.4 GHz | dBi | 0.2 | 2.1 |
| Gain at 3.5 GHz | dBi | −2.9 | −2.2 |
| Gain at 5.8 GHz | dBi | 1.9 | 4.1 |
| Directivity at 2.4 GHz | dBi | 5.8 | 6.1 |
| Directivity at 3.5 GHz | dBi | 4.3 | 4.6 |
| Directivity at 5.8 GHz | dBi | 7.8 | 7.9 |
| Radiation efficiency at 2.4 GHz | % | 27.1 | 40.0 |
| Radiation efficiency at 3.5 GHz | % | 18.9 | 20.9 |
| Radiation efficiency at 5.8 GHz | % | 26.0 | 41.8 |

The reflection coefficient of the baseline and the final design is compared in Fig. 10.

Figure 10 shows the change that matters most. In panel (a) the target frequencies are marked with dotted lines and −10 dB with a dashed line; in panel (b) VSWR= 2 is dashed as a common reference for an acceptable match; and in panels (c1)–(c3) the −10 dB region of L10 is shaded. In panel (a), the red baseline curve has strong dips, but they sit at 2.11, 3.80 and 5.37 GHz, away from the dotted target lines. As a result, it is essentially unmatched at 2.4 GHz and 3.5 GHz. The green curve of L10

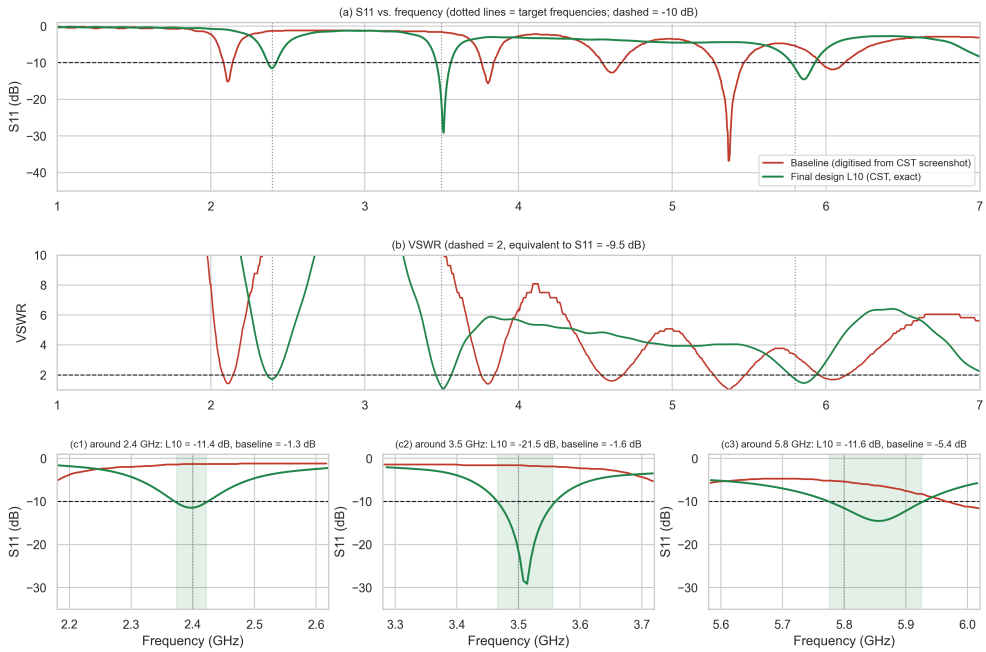
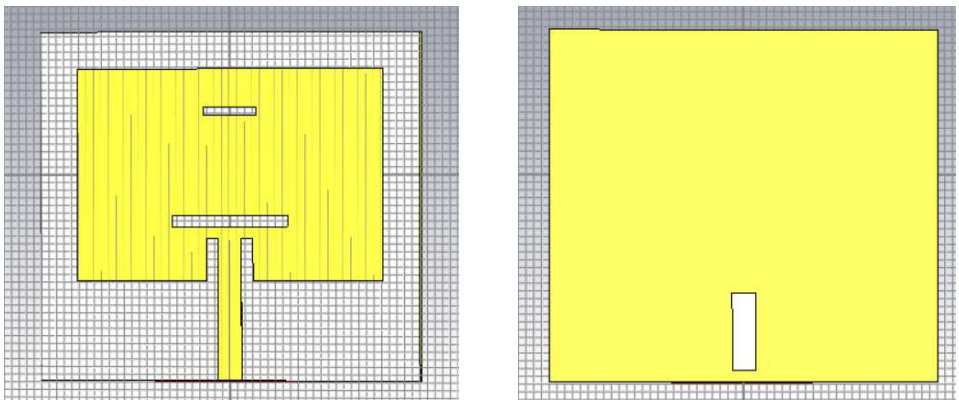



**Fig. 10** Simulated reflection performance of the baseline (digitised from a CST screenshot) and the final design L10 (exact CST export): (a) $S_{11}$ versus frequency; (b) VSWR; (c1)–(c3) zoom around each target frequency.

has dips almost exactly on the first two targets and a broad dip at 5.85 GHz just above the third. The zoom panels quantify this. At 2.4 GHz, L10 reaches −11.4 dB against −1.3 dB for the baseline; at 3.5 GHz, −21.5 against −1.6 dB; and at 5.8 GHz, −11.6 against −5.4 dB. Panel (b) gives the same information as VSWR, which falls from 13.3, 10.9 and 3.3 at the three targets to 1.73, 1.18 and 1.72. Two cautions are needed. The dip in band 3 is shallower than that of the baseline (−14.5 against −41.7 dB): the gain in matching comes from placing the resonances on the targets, not from deeper dips. And the bands are narrow: L10 is below −10 dB over 48, 90 and 150 MHz around the three targets, which covers 29%, 19% and 68% of the 2.4 GHz ISM, n78 and 5.8 GHz ISM bands respectively. The margins from each target to the nearest −10 dB edge are only 22, 34 and 24 MHz.

Figure 11 shows the geometry of L10 in the same views as the baseline of Fig. 1. The overall arrangement is unchanged, which is expected because the search varies five dimensions but keeps the structure. The structure is a patch with the inset feed and two horizontal slots on the top face. The bottom face is a continuous ground plane with the same rectangular DGS notch. Comparing panel (a) with the baseline top view, the patch is visibly wider than it is tall, and the inset notch and the two slots are both shorter. This agrees with the parameter changes in Table 12. The shorter inset moves the feed point closer to the patch edge, where the input impedance is higher, and this is what improves the match at 2.4 GHz. The board footprint follows the patch



(a) (b)

**Fig. 11** Geometry of the final design L10 in CST: (a) top view and (b) bottom view.

dimensions ($W_g = W_p + 6h$, $L_g = L_p + 17.8$ mm), so the overall board is 50.0 mm by 45.3 mm for L10 against 47.6 mm by 47.2 mm for the baseline. The final design has practically the same area (about 2270 against 2250 mm$^2$), so the improvement does not come at the cost of size. The DGS notch itself is unchanged in size.

## 4.8 Gain, efficiency and radiation patterns

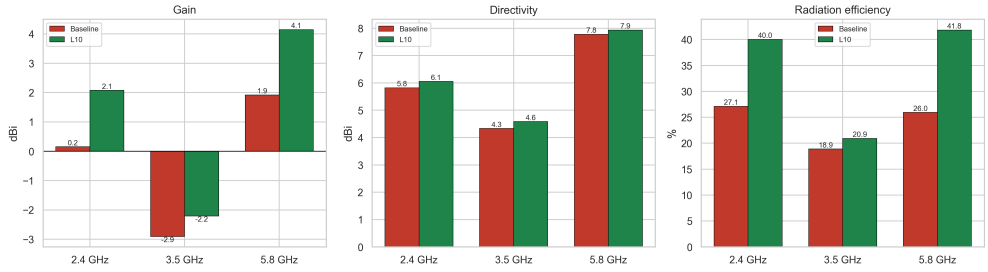
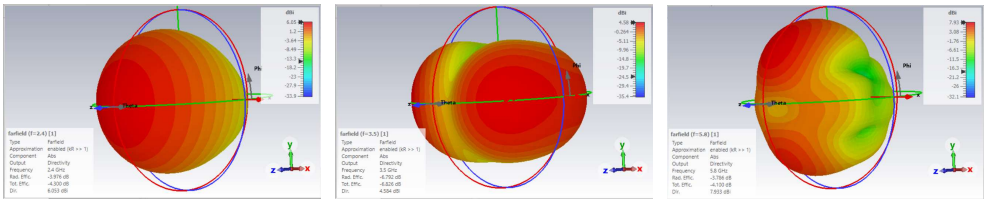



**Fig. 12** Gain, directivity and radiation efficiency of the baseline and of L10 at the three target frequencies (CST far-field results).

Figure 12 compares the three radiation metrics at the target frequencies. Directivity is almost unchanged (5.8, 4.3 and 7.8 dBi for the baseline against 6.1, 4.6 and 7.9 dBi for L10), which is expected, since the radiating aperture is about the same. The gain and the efficiency, however, improve at 2.4 and 5.8 GHz. Gain rises from 0.2 to 2.1 dBi and from 1.9 to 4.1 dBi, and radiation efficiency rises from 27.1% to 40.0% and from 26.0% to 41.8%. At 3.5 GHz the gain is still negative ($-2.2$ dBi, against $-2.9$ dBi for the baseline) and the efficiency is only 20.9%. Equation (6) explains this: with a directivity of 4.6 dBi and an efficiency of 20.9%, the gain is $4.6 - 6.8 = -2.2$ dBi. The low efficiencies are not surprising, since FR-4 has a loss tangent of 0.025 and a resonant

slot adds conductor and dielectric loss. They do, however, show that the improvement in matching does not translate into a high-performance radiator. A substrate with a lower loss tangent is the obvious next step.



(a) 2.4 GHz (b) 3.5 GHz (c) 5.8 GHz

**Fig. 13** Three-dimensional directivity patterns of L10 in CST at (a) 2.4 GHz, (b) 3.5 GHz and (c) 5.8 GHz.

Figure 13 shows the simulated three-dimensional directivity patterns. The colour scale is in dBi and its top value is the peak directivity: 6.05, 4.58 and 7.93 dBi at 2.4, 3.5 and 5.8 GHz. At 2.4 GHz the pattern is a single smooth lobe with no deep nulls, as expected for the fundamental patch mode. At 3.5 GHz it is also a single broad lobe, but with a lower peak, which fits the lower directivity of that band. At 5.8 GHz the pattern is more structured: the main lobe is accompanied by side lobes and shallow nulls, which suggests a more complex current distribution at this frequency. Its peak is also the highest of the three. The information boxes give radiation efficiencies of $-3.98$, $-6.79$ and $-3.79$ dB (40.0, 20.9 and 41.8%) and total efficiencies of $-4.30$, $-6.83$ and $-4.10$ dB. The total efficiency includes the mismatch loss, and it is only slightly below the radiation efficiency, in agreement with the good match at the three frequencies. Only these three-dimensional directivity plots were extracted; principal-plane cuts and half-power beamwidths are left for future work.

## 4.9 Sensitivity to dimensional tolerance

Because the bands are narrow, a small change in geometry could detune the antenna. The tolerance study of Section 3.6 answers this with eight simulations around L10. Table 13 lists the results and Fig. 14 shows the dip shifts and the main effects.

Figure 14 shows in panel (a) that a $\pm 0.15$ mm change in the five dimensions moves the dips by up to 18 MHz in bands 1 and 2 and up to 30 MHz in band 3. Panel (b) shows that the shifts are dominated by few parameters. Band 1 is set by the patch length (main effect $-24$ MHz), band 2 by the patch width ($-26$ MHz) and band 3 by the patch length ($-34$ MHz) and the width ($-14$ MHz). The second slot length $L_{s3}$ has almost no effect in any band (at most 1.5 MHz), which is consistent with its low importance in Fig. 7. $y_0$ and $L_{s2}$ have small effects of up to about 10 MHz. The consequence is visible in Table 13: six of the eight variants still meet all three targets, and all eight meet at least two. The two variants that lose a target both lose band 3, whose dip moves upward by $+30$ and $+18$ MHz and leaves $S_{11}$ at 5.8 GHz at $-9.0$ and $-9.5$ dB. Its margin in L10 is only 24 MHz, so the margin is the practical quantity to watch. Band 1 is the limiting band, since its dip is only about $-11$ dB in every

**Table 13** Tolerance study around L10: geometry (mm), $S_{11}$ (dB) at the three target frequencies, number of bands met and shift of the three dips relative to L10 (bands 1/2/3).

| Run | $L_p$ | $W_p$ | $L_{s2}$ | $L_{s3}$ | $y_0$ | $S_{11}$ 2.4 | 3.5 | 5.8 | Met | Dip shifts (MHz) |
|---|---|---|---|---|---|---|---|---|---|---|
| L10 | 27.542 | 40.446 | 15.217 | 7.091 | 5.477 | −11.4 | −21.5 | −11.6 | 3 | 0 / 0 / 0 |
| T01 | 27.392 | 40.296 | 15.067 | 7.181 | 5.627 | −11.5 | −14.4 | −9.0 | 2 | +12 / +12 / +30 |
| T02 | 27.392 | 40.296 | 15.367 | 7.181 | 5.327 | −10.9 | −15.7 | −10.9 | 3 | +12 / +12 / +18 |
| T03 | 27.392 | 40.596 | 15.067 | 7.001 | 5.627 | −11.5 | −24.0 | −9.5 | 2 | +12 / −12 / +18 |
| T04 | 27.392 | 40.596 | 15.367 | 7.001 | 5.327 | −11.0 | −29.2 | −11.5 | 3 | +12 / −18 / +6 |
| T05 | 27.692 | 40.296 | 15.067 | 7.001 | 5.327 | −11.2 | −16.7 | −13.7 | 3 | −6 / +6 / −6 |
| T06 | 27.692 | 40.296 | 15.367 | 7.001 | 5.627 | −10.4 | −15.2 | −12.1 | 3 | −18 / +12 / −12 |
| T07 | 27.692 | 40.596 | 15.067 | 7.181 | 5.327 | −11.4 | −31.2 | −14.9 | 3 | −6 / −18 / −18 |
| T08 | 27.692 | 40.596 | 15.367 | 7.181 | 5.627 | −10.6 | −28.1 | −12.7 | 3 | −18 / −12 / −30 |

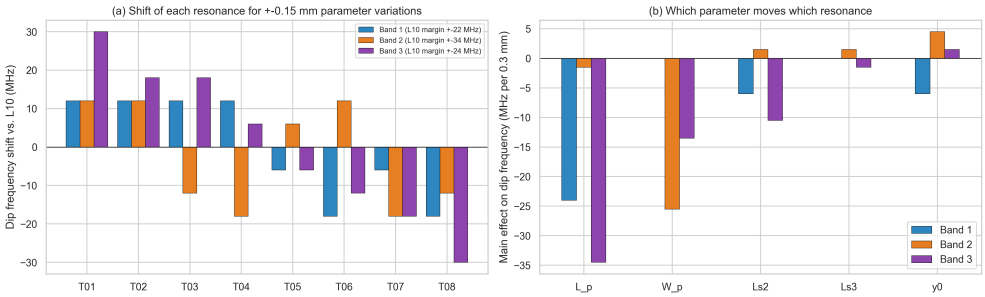



**Fig. 14** Sensitivity of L10 in the fractional-factorial tolerance study: (a) shift of the dip frequency in each band for the eight runs T01–T08, (b) main effect of each parameter on the dip frequency of each band, in MHz per 0.3 mm change.

variant. The 22 MHz first-band margin of L10 is smaller than the detuning that may be caused by the permittivity spread of FR-4 and fabrication tolerance, which was not quantified here. As a result, the result is not a guarantee of measured performance.

## 4.10 Discussion and limitations

Several points follow from the results. First, the ML surrogates were useful but not sufficient. They predicted the fundamental resonance almost perfectly, screened poor designs well and narrowed the search to a promising region. However, they could not predict the second and third resonances accurately enough to place them, and the last step needed local simulation. This is in line with other studies that use surrogates to reduce, not to remove, the number of full-wave simulations [21, 23, 26]. Second, the exact-frequency criterion changed the picture: all eight first-stage candidates satisfied the window-minimum test, but only three met any target at the required frequency. Third, the data-consistency check was essential. Had the first campaign been used, the conclusion would have been that the outputs were unlearnable. Dataset checks, such as comparing repeated geometries and testing a known physical trend, are cheap and should precede any surrogate training.

The main limitations are as follows. All results come from simulation and nothing was fabricated or measured. The final design is narrow-band, its first-band margin is thin, and its gain and efficiency are modest, with negative gain at 3.5 GHz. The dataset stores the deepest dip of each window rather than $S_{11}$ at the target frequency. As a result, the surrogates were not trained on the quantity that the final requirement uses. The test set has 95 designs and a single split was used, so small differences between models cannot be resolved. Only five geometric parameters were varied and the final design lies near two of the limits. The baseline curve and the first-batch $S_{11}$ values were digitised from screenshots with an accuracy of about $\pm 0.2$ dB and 5 MHz. The curves for the final design and the tolerance study, by contrast, are exact exports.

# 5 Conclusions

This paper has presented a machine-learning-assisted workflow for a compact triple-band microstrip patch antenna on FR-4, targeting the 2.4 GHz ISM, 3.5 GHz 5G n78 and 5.8 GHz ISM bands. The antenna is a dual-slot, inset-fed patch with a defected ground structure, parametrised with five geometric variables. An 805-geometry Latin Hypercube plan was simulated in CST Studio Suite to yield 630 usable samples with 15 outputs each. Random forest, XGBoost and a neural network were trained on this data, with electrical-length features added for XGBoost and for an $S_{11}$-only neural network in a deployable two-stage cascade. On a held-out test set of 95 designs, the engineered-feature XGBoost model reached the highest mean $R^2$ across the 15 outputs (0.72). This compares with 0.70 for the raw neural network, 0.68 for raw XGBoost and 0.67 for random forest. Broken down by output, $R^2$ was about 0.44 for $S_{11}$, 0.71 for resonant frequency and 0.76 to 0.84 for directivity, gain and radiation efficiency. The gap between the ANN and XGBoost was within statistical noise, and the benefit of the engineered features was not statistically established at this sample size. Even so, the engineered-feature XGBoost model remains the more practical choice overall. It is the only configuration trained for every output rather than $S_{11}$ alone, and its accuracy is not distinguishably worse than the neural network's. As screening tools, the surrogates proved clearly informative. AUC values ranged from 0.93 for the raw neural network to 0.99 for the $S_{11}$-only engineered neural network, well above an always-pass rule. Guided by these surrogates, a differential-evolution search proposed eight candidates and a 24-design local batch. The final design, L10, emerged from this batch: it meets $S_{11} \leq -10$ dB at 2.4, 3.5 and 5.8 GHz ($-11.4$, $-21.5$ and $-11.6$ dB), where the baseline meets none of them. The corresponding VSWR values are 1.73, 1.18 and 1.72. L10 also raises the gain at 2.4 and 5.8 GHz by about 1.9 and 2.2 dBi, and the radiation efficiency by 13 and 16 percentage points. A tolerance study with $\pm 0.15$ mm variations showed that six of eight variants still meet all three targets. It also identified the patch length and width as the parameters that move the resonances most. Notably, the surrogates guided this search without ever predicting L10 directly, since the second and third resonances remain poorly predicted ($R^2$ of 0.62 and 0.51). The final design was therefore reached through local simulation rather than through surrogate inference. Some caution is warranted alongside these results, however. The final antenna is narrow-band, with $-10$ dB widths of only 48, 90 and 150 MHz. Its

gain at 3.5 GHz is still negative, and its efficiency reaches at most 21–42%. Everything reported here is simulated. In addition, a first simulation campaign of the same plan had to be discarded after identical geometries produced unrelated outputs; the cause is a licence-edition difference, a free, mesh-capped Learning Edition for the discarded campaign against an uncapped commercial licence for the retained one (Section 4.2). Each of these limitations points to a fairly specific next step. The 22 MHz first-band margin is the thinnest in the design and has never been checked against real material variation. Fabricating and measuring L10 with a vector network analyser would show directly whether the simulated match survives the permittivity spread of FR-4 and ordinary fabrication tolerance. Section 4.9 raised this question but could not quantify it. The dataset trains on the deepest dip within a search window rather than $S_{11}$ at the exact target frequency. As a result, all eight first-stage candidates passed the window-minimum screen even though only three met any target at the required frequency. Only one of the 24 local-batch designs met all three (Section 4.6). Re-labelling the training data with $S_{11}$ sampled at the target frequencies, or with band coverage, would align the surrogates with the quantity the design goal actually uses. This should reduce the roughly 40 verification simulations this mismatch currently costs. Likewise, the cost function of Eq. (13) rewards only a deep, well-placed match. This is consistent with L10's negative gain at 3.5 GHz and its radiation efficiencies of only 18.9–41.8%. Adding gain and efficiency terms to the cost, and testing a substrate with a lower loss tangent than FR-4's 0.025, should target this shortfall more directly. L10's inset depth and second slot length also sit at or near the lower limits of Table 2 (Section 4.7). This suggests that the true optimum may lie outside the explored design space. Widening that space, and adding slot position, slot width and feed gap as free parameters, would test whether this bound is genuinely binding. It could also widen the narrow $-10$ dB bandwidths (48-150 MHz), which presently cover only 19–68% of the three bands. The single 95-design test split used throughout also left most model differences statistically indistinguishable (Table 8). Repeated cross-validation over multiple splits would therefore need to precede any firm claim that XGBoost outperforms the ANN, or that the engineered features genuinely help. Bands 2 and 3 remain the surrogates' weakest point ($R^2$ of 0.62 and 0.51 for resonant frequency, against 0.99 for band 1). Uncertainty-aware sampling, for instance with Gaussian-process surrogates that target new simulations at the least-certain geometries, would focus the simulation budget precisely where the current fixed Latin Hypercube plan under-serves. Finally, although the Round 2 inconsistency is now attributed to a mesh-capped free licence edition (Section 4.2), a repeat-geometry control, run and checked at the outset of every future campaign before any surrogate is trained, would still help. It would catch a similar licence, mesh or export difference before it costs another discarded campaign. Taken together, these steps would let the workflow reduce the number of full-wave simulations needed for multiband antenna design while keeping the final decision tied to verified simulation.

## Declarations

- **Ethics, Consent to Participate and Consent to Publish declarations**: Not applicable.

- **Funding**: This research did not receive any grant or funding from public, commercial, or not-for-profit sectors.

- **Data availability**: The datasets generated during and/or analysed during the current study are available from the corresponding author on reasonable request.

- **Conflict of interest**: No conflict of interest.

- **Clinical trial number**: Not applicable.

- **Author contribution**:
  P.T.B. Halweendo: Conceptualisation, Antenna design and simulation, dataset generation, machine-learning implementation, analysis and manuscript preparation.
  Srinu Sesham: Supervision, Results verification and testing, Guidance on methodology, and manuscript review.
  Clement Temaneh Nyah: Performance validation and revising the manuscript.

## References

[1] Kawale, S.S., Zade, P.L., Khade, S., Dorge, P., Dorle, S., Jumle, P.: Design and Analysis of a Multiband Antenna for Wireless Applications. In: 2025 1st International Conference on Radio Frequency Communication and Networks (RFCoN), Thanjavur, India, pp. 1–5 (2025). https://doi.org/10.1109/RFCoN62306.2025.11085089

[2] Nepaya, L., Srinu, S., F. M. S, A.: Reconfigurable quad-band filter based on reactance transform method for wideband cognitive sensor applications. In: 2022 IEEE 19th India Council International Conference (INDICON), Kochi, India, pp. 1–5 (2022). https://doi.org/10.1109/indicon56171.2022.10039727

[3] Imam-Fulani, Y.O., Faruk, N., Sowande, O.A., Abdulkarim, A., Alozie, E., Usman, A.D., *et al.*: 5G Frequency Standardization, Technologies, Channel Models, and Network Deployment: Advances, Challenges, and Future Directions. Sustainability **15**(6), 5173 (2023) https://doi.org/10.3390/su15065173

[4] 3GPP: NR; Base Station (BS) radio transmission and reception. Technical Specification TS 38.104, version 19.4.0, Release 19 (published by ETSI as TS 138 104 V19.4.0), 3rd Generation Partnership Project (April 2026)

[5] IEEE: IEEE Std 802.11-2020: IEEE Standard for Information Technology – Telecommunications and Information Exchange between Systems – Local and

Metropolitan Area Networks – Specific Requirements – Part 11: Wireless LAN Medium Access Control (MAC) and Physical Layer (PHY) Specifications (2021). https://doi.org/10.1109/IEEESTD.2021.9363693

[6] Kadam, S.A., Mohite, D.D.: Design and performance evaluation of microstrip fractal multiband patch antenna for wireless communication applications. Engineering Research Express **7**(3), 035307 (2025) https://doi.org/10.1088/2631-8695/adea34

[7] Balamurugan C, Arun Samuel T.S., Merlin Gilbert Raj S, Pricilla Mary S, Sharon Geege A: Enhancing gain and bandwidth in a multiband microstrip patch antenna through L-slot and partial ground plane integration. Scientific Reports **15**(1), 29083 (2025) https://doi.org/10.1038/s41598-025-13947-8

[8] Pushadapu, P., Rao, G.S., Thota, P., Parisa, P., Indhu, V.: A Multiband High-Performance L-Shaped Microstrip Patch Antenna with DGS For 5G Applications. International Journal of Innovative Research in Engineering and Management **12**(2), 75–76 (2025) https://doi.org/10.55524/ijirem.2025.12.2.12

[9] Maaroufi, I., EL Beqal, A., Nasraoui, H., Serbouti, M., Benhala, B.: Triple-band double-T monopole antenna: Design and experimental validation. Progress in Engineering Science **3**(4), 100377 (2026) https://doi.org/10.1016/j.pes.2026.100377

[10] Garg, R., Bhartia, P., Bahl, I., Ittipiboon, A.: Microstrip Antenna Design Handbook. Artech House, Boston, MA (2001)

[11] Kumar, A., Dewan, B., Khandelwal, A., Shrivastava, K.: On the devolvement of fractal antenna for IoT applications. Engineering Research Express **5**(3), 035026 (2023) https://doi.org/10.1088/2631-8695/acebb8

[12] Nusrat, T., Roy, S.: On the Design of a Multiband Microstrip Patch Antenna by Introducing a Defected Ground Structure. In: 2022 IEEE Research and Applications of Photonics in Defense Conference (RAPID), pp. 1–2 (2022). https://doi.org/10.1109/rapid54472.2022.9911261

[13] Boursianis, A.D., Papadopoulou, M.S., Pierezan, J., Mariani, V.C., Coelho, L.S., Sarigiannidis, P., *et al.*: Multiband Patch Antenna Design Using Nature-Inspired Optimization Method. IEEE Open Journal of Antennas and Propagation **2**, 151–162 (2021) https://doi.org/10.1109/ojap.2020.3048495

[14] Fertas, F., Fertas, K., Denidni, T.A., Challal, M.: Design of miniaturized tri-band antenna based on differential evolution algorithm. Microwave and Optical Technology Letters **65**(3), 930–935 (2023) https://doi.org/10.1002/mop.33579

[15] El-Hakim, H., Mohamed, H.A.: Synthesis of a Multiband Microstrip Patch

Antenna for 5G Wireless Communications. Journal of Infrared, Millimeter, and Terahertz Waves **44**(9-10), 752–768 (2023) https://doi.org/10.1007/s10762-023-00937-y

[16] Khan, M.M., Hossain, S., Mozumdar, P., Akter, S., Ashique, R.H.: A review on machine learning and deep learning for various antenna design applications. Heliyon **8**(4), 09317 (2022) https://doi.org/10.1016/j.heliyon.2022.e09317

[17] Sarker, N., Podder, P., Mondal, M.R.H., Shafin, S.S., Kamruzzaman, J.: Applications of Machine Learning and Deep Learning in Antenna Design, Optimization, and Selection: A Review. IEEE Access **11**, 103890–103915 (2023) https://doi.org/10.1109/access.2023.3317371

[18] Belen, A., Tari, O., Mahouti, P., Belen, M.A., Çalışkan, A.: Surrogate-Based Design Optimization of Multi-Band Antenna. The Applied Computational Electromagnetics Society Journal (ACES) (2022) https://doi.org/10.13052/2022.aces.j.370104

[19] Zou, H., Zeng, S., Li, C., Ji, J.: A survey of machine learning and evolutionary computation for antenna modeling and optimization: Methods and challenges. Engineering Applications of Artificial Intelligence **138**, 109381 (2024) https://doi.org/10.1016/j.engappai.2024.109381

[20] Pusuluri, V.B., Prasad, A.M., Darimireddy, N.K.: Design of 5g dual band antenna and optimization using machine learning techniques. Indian Journal of Science and Technology **18**(30), 2442–2452 (2025) https://doi.org/10.17485/ijst/v18i30.910

[21] Wu, Q., Chen, W., Yu, C., Wang, H., Hong, W.: Machine-Learning-Assisted Optimization for Antenna Geometry Design. IEEE Transactions on Antennas and Propagation **72**(3), 2083–2095 (2024) https://doi.org/10.1109/tap.2023.3346493

[22] Aliyu Babale, S., Kim Geok, T., Kamal Abdul Rahim, S., Pao Liew, C., Musa, U., Fatihu Hamza, M., *et al.*: Machine Learning-Based Optimized 3G/LTE/5G Planar Wideband Antenna With Tri-Bands Filtering Notches. IEEE Access **12**, 80669–80686 (2024) https://doi.org/10.1109/access.2024.3407371

[23] Palandöken, M., Belen, A., Tari, O., Mahouti, P., Mahouti, T., Belen, M.A.: Computationally Efficient Design Optimization of Multiband Antenna Using Deep Learning–Based Surrogate Models. International Journal of RF and Microwave Computer-Aided Engineering **2024**(1), 5442768 (2024) https://doi.org/10.1155/mmce/5442768

[24] Gupta, A., Karahan, E.A., Bhat, C., Sengupta, K., Khankhoje, U.K.: Tandem Neural Network Based Design of Multiband Antennas. IEEE Transactions on Antennas and Propagation **71**(8), 6308–6317 (2023) https://doi.org/10.1109/tap.2023.3276524

[25] Chen, S., Sun, G.-H., Wang, K.: Inverse Design of Microstrip Antennas Based on Deep Learning. Electronics **14**(13), 2510 (2025) https://doi.org/10.3390/electronics14132510

[26] Koziel, S., Pietrenko-Dabrowska, A., Leifsson, L.: Antenna optimization using machine learning with reduced-dimensionality surrogates. Scientific Reports **14**(1), 21567 (2024) https://doi.org/10.1038/s41598-024-72478-w

[27] Haque, M.A., Rahman, M.A., Al-Bawri, S.S., Yusoff, Z., Sharker, A.H., Abdulkawi, W.M., *et al.*: Machine learning-based technique for gain and resonance prediction of mid band 5G Yagi antenna. Scientific Reports **13**(1), 12590 (2023) https://doi.org/10.1038/s41598-023-39730-1

[28] Dou, J., Gong, H., Chen, H., Chen, Y., Shen, T., Song, J.: A Reinforcement Learning-Based Image Mapping-Topology Optimization for Antenna Design. IEEE Antennas and Wireless Propagation Letters **24**(7), 1759–1763 (2025) https://doi.org/10.1109/lawp.2025.3546348

[29] Rafidul, S., Akinsolu, M.O., Liu, B., Kumar, C., Guha, D.: Machine Learning-Assisted Microstrip Antenna Design Featuring Extraordinary Polarization Purity. IEEE Antennas and Wireless Propagation Letters **24**(4), 1008–1012 (2025) https://doi.org/10.1109/lawp.2024.3524249

[30] Kumar, A., Khan, T., Sarkar, D.: Forward-inverse-hybrid modeling of microstrip antennas using decision tree-based machine learning algorithms for space communication. AEU - International Journal of Electronics and Communications **191**, 155662 (2025) https://doi.org/10.1016/j.aeue.2025.155662

[31] Dwivedi, A.K., Singh, V., Alzahrani, Y., Chaitanya, R.K., Singh, S.K., Singh, S., *et al.*: A taguchi neural network–based optimization of a dual-port, dual-band MIMO antenna encompassing the 28/34 GHz millimeter wave regime. Scientific Reports **15**(1), 6026 (2025) https://doi.org/10.1038/s41598-025-90103-2

[32] Sarvesan, S., Reddy, M.G., Karthikeyan, S.S., Sekhar, P.K.: Low-cost fabrication and comparative evaluation of machine learning algorithms for flexible PDMS-based hexagonal patch antenna. Scientific Reports **15**(1), 30187 (2025) https://doi.org/10.1038/s41598-025-15678-2

[33] Dhar, J.P., Nishiyama, E., Toyoda, I.: Square-Ring Microstrip Antenna Design Using Efficient 2-Layer Artificial Neural Network. International Journal on Communications Antenna and Propagation (IRECAP) **15**(6), 326 (2025) https://doi.org/10.15866/irecap.v15i6.26584

[34] Nirob, J.H., Das, I., Nahin, K.H., Tiang, J.-J., *et al.*: High performance grid structured MIMO antenna with regression machine learning for high-speed sub THz and THz 6G IoT applications. Scientific Reports **15**(1), 31410 (2025) https://doi.org/10.1038/s41598-025-15773-4

[35] Rahman, M.A., Al-Bawri, S.S., Abdulkawi, W.M., Aljaloud, K., Islam, M.T.: A unique SWB multi-slotted four-port highly isolated MIMO antenna loaded with metasurface for IOT applications-based machine learning verification. Engineering Science and Technology, an International Journal **50**, 101616 (2024) https://doi.org/10.1016/j.jestch.2024.101616

[36] Al-Hiti, A.S., Ahmed, A.K., Mhmood, S.H., Hamdallah, B.I.: Broadband and multiband millimeter wave microstrip patch antenna for 5G and 6G applications. Journal of Umm Al-Qura University for Engineering and Architecture **16**(3), 720–731 (2025) https://doi.org/10.1007/s43995-025-00161-w

[37] Rajeshwar, B., VANKDOTH, K., THATIKONDA, A.: Design and Simulation of Multiband Microstrip Patch Antenna for Wireless Applications Using HFSS. Acta Mechanica et Automatica **19**(3), 505–513 (2025) https://doi.org/10.2478/ama-2025-0058

[38] Grinsztajn, L., Oyallon, E., Varoquaux, G.: Why do tree-based models still outperform deep learning on tabular data? https://arxiv.org/abs/2207.08815 (2022)

[39] Srinu, S., K, V.S.K., Nepaya, L., Sabat, S.L., F.M.S, A.: System on Chip implementation of dual-band spectrum sensing using energy detection algorithm. In: 2022 IEEE 19th India Council International Conference (INDICON), Kochi, India, pp. 1–6 (2022). https://doi.org/10.1109/indicon56171.2022.10039768

[40] Sesham, S., Suresh, N., Chembe, D.K.: Development of signal processing and machine learning methods for spectrum sensing using autocorrelation features. Discover Applied Sciences **7**(11), 1237 (2025) https://doi.org/10.1007/s42452-025-07787-4

[41] Shahriar, S.M., Khan, T.F., Sabreen, A., Hossain, M.A., Barua, N.: Machine Learning-Assisted Return Loss Optimization for Quad-Band Microstrip Antenna for 5G and Wifi-6/7 Applications. In: 2025 International Conference on Quantum Photonics, Artificial Intelligence, and Networking (QPAIN), pp. 1–6 (2025). https://doi.org/10.1109/qpain66474.2025.11171684

[42] Bennet, M.A., Selvakani, R.: Optimization of High-Performance Microstrip Antenna Design Through Machine Learning-Enhanced Parameter Sweeping Techniques. In: 2025 8th International Conference on Circuit, Power & Computing Technologies (ICCPCT), pp. 920–925 (2025). https://doi.org/10.1109/iccpct65132.2025.11176481

[43] Balanis, C.A.: Antenna Theory: Analysis and Design, 4th edn. Wiley, Hoboken, NJ (2016)

[44] Hammerstad, E., Jensen, O.: Accurate Models for Microstrip Computer-Aided Design. In: 1980 IEEE MTT-S International Microwave Symposium Digest, pp.

407–409 (1980). https://doi.org/10.1109/mwsym.1980.1124303

[45] McKay, M.D., Beckman, R.J., Conover, W.J.: A Comparison of Three Methods for Selecting Values of Input Variables in the Analysis of Output from a Computer Code. Technometrics **21**(2), 239–245 (1979) https://doi.org/10.2307/1268522

[46] Clemens, M., Weiland, T.: Discrete electromagnetism with the finite integration technique. Progress in Electromagnetics Research **32**, 65–87 (2001) https://doi.org/10.2528/PIER00080103

[47] Dassault Systèmes: CST Studio Suite: Electromagnetic Field Simulation Software (Time Domain Solver), versions 2023 and 2026. https://www.3ds.com/products/simulia/cst-studio-suite

[48] Breiman, L.: Random Forests. Machine Learning **45**(1), 5–32 (2001) https://doi.org/10.1023/a:1010933404324

[49] Chen, T., Guestrin, C.: XGBoost. In: Proceedings of the 22nd ACM SIGKDD International Conference on Knowledge Discovery and Data Mining, pp. 785–794 (2016). https://doi.org/10.1145/2939672.2939785

[50] Virtanen, P., Gommers, R., Oliphant, T.E., Haberland, M., Reddy, T., Cournapeau, D., *et al.*: SciPy 1.0: fundamental algorithms for scientific computing in Python. Nature Methods **17**(3), 261–272 (2020) https://doi.org/10.1038/s41592-019-0686-2